UC Santa Cruz

UC Santa Cruz Previously Published Works

Title

Binary pseudo-random patterned structures for modulation transfer function calibration and resolution characterization of a full-field transmission soft x-ray microscope

Permalink

https://escholarship.org/uc/item/9f27n0qw

Journal

Review of Scientific Instruments, 86(12)

ISSN

0034-6748

Authors

Yashchuk, VV

Fischer, PJ

Chan, ER

et al.

Publication Date

2015-12-01

DOI

10.1063/1.4936752

Peer reviewed

eScholarship.org Powered by the California Digital Library
University of California

Binary pseudo-random patterned structures for modulation transfer function calibration and resolution characterization of a full-field transmission soft x-ray microscope

V. V. Yashchuk,[1,a] P. J. Fischer,[2,3] E. R. Chan,[1] R. Conley,[4,5] W. R. McKinney,[b] N. A. Artemiev,[c] N. Bouet,[5] S. Cabrini,[6] G. Calafiore,[7] I. Lacey,[1] C. Peroz,[7] and S. Babin[7]

[1]*Advanced Light Source Berkeley, Lawrence Berkeley National Laboratory, California, 94720, USA*

[2]*Center for X-Ray Optics, Lawrence Berkeley National Laboratory, California, 94720, USA*

[3]*Physics Department, University of California Santa Cruz, Santa Cruz, California 94056*

[4]*Advance Photon Source, Argonne National Laboratory, Argonne, Illinois, 60439, USA*

[5]*National Synchrotron Light Source II, Brookhaven National Laboratory, Upton, New York 11973, USA*

[6]*Molecular Foundry, Lawrence Berkeley National Laboratory, California, 94720, USA*

[7]*aBeam Technologies, Inc., Hayward, California, 94541, USA*

We present a modulation transfer function (MTF) calibration method based on binary pseudo-random (BPR) one-dimensional sequences and two-dimensional arrays as an effective method for spectral characterization in the spatial frequency domain of a broad variety of metrology instrumentation, including interferometric microscopes, scatterometers, phase shifting Fizeau interferometers, scanning and transmission electron microscopes, and at this time, x-ray microscopes. The inherent power spectral density of BPR gratings and arrays, which has a deterministic white-noise-like character, allows a direct determination of the MTF with a uniform sensitivity over the entire spatial frequency range and field of view of an instrument. We demonstrate the MTF calibration and resolution characterization over the full field of a transmission soft x-ray microscope using a BPR multilayer (ML) test sample with 2.8-nm fundamental layer thickness. We show that beyond providing a direct measurement of the microscope's MTF, tests with the BPRML sample can be used to fine tune the instrument's focal distance. Our results confirm the universal character of the method indicating its applicability to a large variety of metrology instrumentation with spatial wavelength bandwidths from a few nanometers to hundreds of millimeters.

[a] Author to whom correspondence should be addressed. Electronic mail: VVYashchuk@lbl.gov.

[b] This research was performed while W. R. McKinney was at Advanced Light Source, Lawrence Berkeley National Laboratory, Berkeley, CA, 94720, USA.

[c] This research was performed while N. A. Artemiev was at Advanced Light Source, Lawrence Berkeley National Laboratory, Berkeley, CA, 94720, USA.

I. INTRODUCTION

Metrology devices which produce images of a topographical object, for example, images of surface morphology measured with an optical microscope, or images of a bulk material structure recorded with transmission x-ray and electron microscopes, do not reproduce the shape of an object with 100% fidelity. The probes used, optical light, x-rays, electrons, or a pointed material tip as in a scanning probe microscope, have limitations. Photons (visual light and x-rays) are limited by diffraction to approximately the wavelength; electrons are limited by their energy and subsequent aberrations in electromagnetic focusing systems; scanning probe tips cannot be infinitely sharp. In addition to the probe, the finite size of a pixel in the instrumental detector (for example, a CCD camera) can also limit the quality of the image. Key for further progress in many areas of nanoscience and in nanofabrication relying on high resolution metrology is the development of reliable experimental methods for precision quantitative characterization and calibration of appropriate high resolution metrology instruments, such as electron and x-ray microscopes.

In the most rigorous metrology with a variety of surface profilometers and microscopes for spectral characterization of surface height properties in the frequency domain, a statistical description based on power spectral density (PSD) distributions is widely used.[1-5] Reliability of the PSD data relies on experimental methods available for comprehensive measurement of the spatial frequency response of the instrument that is usually described with a modulation transfer function (MTF).[6] Physically, the instrumental MTF is the amplitude response of the imaging system to sine-wave-like objects of different spatial frequencies. The limited spatial resolution of the system results in a decrease, with increase of the object's spatial frequency, in the modulation amplitude of the image relative to that of the object.

To the extent that the response of the instrument can be characterized as a linear system, the measured PSD is a product of the PSD inherent for the sample, PSD_{sample}, and the MTFs of the individual components (objective, detector, etc.) of the instrument:

$$PSD_{measured} = PSD_{sample} \times MTF^2 . \quad (1)$$

The MTF in Eq. (1) is the total MTF of the instrument. It can be experimentally determined by comparing the measured PSD distribution of a test surface to the corresponding ideal PSD distribution, which is numerically

simulated or found from PSD measurements with an instrument with significantly higher resolution. The square root of the ratio of the measured PSD distribution divided by the ideal PSD distribution gives the MTF of the instrument.

A number of methods for MTF measurements have been developed, see, for example, Refs.[6-10] and references therein. The effectiveness of a given method critically hinges on the appropriate choice of the test sample. The major requirements to the test sample when used as a certified MTF standard are as follows. First, it should be suitable for calibration over the entire instrumental field of view with a uniform sensitivity to the MTF over the entire spatial frequency range up to the highest (Nyquist) frequency of the instrument. Second, in order to be used as a certified standard, the MTF test sample should satisfy the conditions of ease of specification, reproducibility, and repeatability. Third, the accuracy of the MTF calibration should have a reasonably low sensitivity to possible fabrication imperfections of the sample. Most of the common test patterns used in MTF measurements, including knife-edge sources (step height standards), bar targets, sinusoidal surfaces, periodic and quasi-periodic patterns, white noise patterns, and random reference specimens, fail to meet some or all of these requirements.

Recently, an MTF calibration technique based on binary pseudo-random (BPR) one-dimensional (1D) sequences and two-dimensional (2D) arrays has been developed and patented.[11,12] The technique has been proven to be an effective method for spectral characterization in the spatial frequency domain of a broad variety of metrology instrumentation, including interferometric microscopes, scatterometers, phase shifting Fizeau interferometers, as well as scanning and transmission electron microscopes (SEM and TEM, respectively).[12-18]

BPR sequences and arrays are 1D and 2D patterns, respectively, of statistically independent and uniformly distributed binary elements (1's and 0's or -1's and +1's). We use the term 'pseudo-random' to emphasize that the distributions are generated by mathematically precise rules to be random in a mathematically strong sense.[19-21] Alternatively, such sequences are referred to in the literature as pseudo-noise sequences or m-sequences.[19] Specific methods for generation of pseudo-random sequences[22-23] were developed in connection with communication and encryption processes,[24] acoustics,[25] and pseudo-random chopping of a beam in time-of-flight experiments with slow neutrons[26-31] and molecular beams.[32-34] A maximum duty cycle (relative number of 1's and 0's) of approximately 50% is obtained with a maximum-length pseudo-random sequence (MLPRS).[23,32,33] A sequence $\{a_i\}$ of elements, $i = 0, 1, \cdots, N-1$, $N = 2^n - 1$, where n is an integer, is qualified as a MLPRS, if (i) the autocorrelation of the sequence sums to 2^{n-1} and (ii) the sequence is 'almost' uncorrelated. The conditions (i) and (ii) are very natural for a purely random sequence, or white noise that consists entirely of uncorrelated binary elements with a delta-

function-like correlation function. According to the Wiener-Khinchin theorem,[35] the PSD of a sequence with a delta-function-like correlation function is a frequency independent white-noise-like distribution. The 1D BPR sequences used in this publication were generated using the algorithm described in detail in Ref.[23]

Two-dimensional analogues to 1D BPR sequences are designated as uniformly redundant arrays (URA). URAs are widely used as optimal mask patterns for coded aperture imaging techniques.[20] Analogous to the time-of-flight technique based on 1D BPR sequence chopping,[25-34] an imaging technique based on the 2D URAs allows one to obtain a better signal-to-noise ratio, keeping the high angular resolution characteristic of a single pinhole aperture.[36,37] Similar to 1D BPR sequences, the URAs possess both high throughput (50%) and a delta-function-like cyclical autocorrelation function that corresponds to a flat 2D PSD spectrum. Due to the similarity, we employ the term BPR array rather than URA.

Unlike most conventional test surfaces, the inherent PSD of BPR gratings and arrays has a deterministic white-noise-like character. This allows a direct determination of the MTF with a uniform sensitivity over the entire spatial frequency range of an instrument [compare with Eq. (1)].

The universal character of the approach based on BPR test samples, suitable to characterize essentially different instruments, is ensured by the similarity of specification of the test samples as sets (1D sequences, or 2D arrays) of pseudo-randomly distributed elements with a binary (two-level) physical property such as two height levels or two materials with different physical properties, such as x-ray and electron beam transmission, reflectivity, electrical conductivity, magnetic permeability, etc. – Fig. 1.

Figures 1a and 1b illustrate the design of test surfaces, a 1D BPR grating and a 2D BPR array, with 1D and 2D BPR height distributions, respectively. The pitch of the grid or the fundamental size of the pattern (width of the smallest element of the pattern), Δ, determines the inherent Nyquist frequency of the BPR pattern, $f_N = 1/2\Delta$. For lower spatial frequencies, the inherent PSD is limited by the whole size of the array, $L_X = r\Delta$ and $L_Y = s\Delta$ for the two orthogonal directions, $f_X = 1/(r\Delta)$ and $f_Y = 1/(s\Delta)$, respectively.

Figure 1c shows a design of a BPR multilayer (ML) test sample used for measurements with electron microscopes.[17,18] A BPRML sample is a multilayer structure consisting of two materials (marked with indexes 0 and 1) with significantly different contrast when observed with an electron microscope. In order to serve as a test sample for MTF calibration of a SEM or a TEM, the layers of the two materials are pseudo-randomly distributed according to a binary pseudo-random sequence, similar to ones used for fabrication of BPR gratings (Fig. 1a) and applied to

1D MTF calibration of interferometric microscopes[12] and optical scatterometers.[14] In the BPRML case, the thickness of a particular layer of the material with index 0 (1) is equal to the fundamental layer thickness of the multilayer, Δt , multiplied by the number of adjacent 0's (1's) in the BPR sequence used for the multilayer generation.

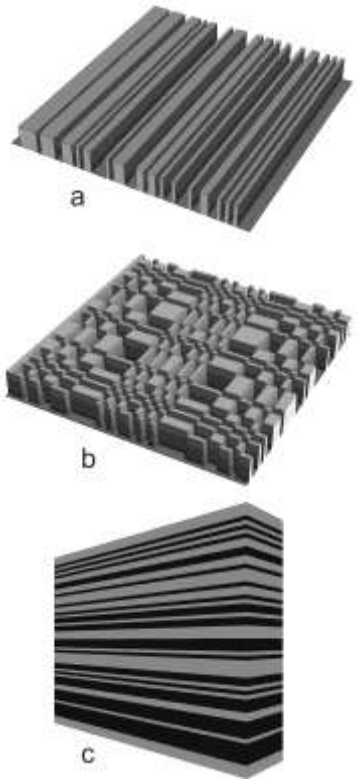

FIG. 1. One dimensional and two dimension binary pseudo-random test objects: (a) grating, (b) array, and (c) multilayer sample.

The binary height of the pattern (Figs. 1a and 1b) and the binary contrast of the MPRML sample materials (Fig. 1c) determine the amplitude of the array's inherent PSD spectrum. Because the PSD from a BPR grating or array is a result of the distribution of the elements, it is not particularly sensitive to the shape or roughness of the sample grooves or interfaces between the layers.[16] This ensures the high accuracy of the MTF measurements with the BPR test samples.

Here, we report on an advanced expansion of the application range of the method to the MTF calibration and resolution characterization using the full-field transmission soft x-ray microscope (TXM) XM-1, at beamline 6.1.2 at the Advanced Light Source (ALS) in Berkeley, CA.[38] In Sec. 2, we describe in details the development of the BPRML test sample with 2.8-nm fundamental layer thickness used for measurements with the x-ray microscope. The measurement procedure, data processing, and the results of measurements of the XM-1 MTF are discussed in Sec. 3. We show that beyond providing a direct measurement of the microscope's MTF, tests with the BPRML

sample can be used to fine tune the instrument's focal distance. The investigations confirm the universal character of the method that makes it applicable to a large variety of metrology instrumentation with spatial wavelength bandwidths from a few nanometers to hundreds of millimeters.

II. FABRICATION AND CHARACTERIZATION OF THE BPRML TEST SAMPLE

Similarly to the characterization of electron microscopes,[17,18] the BPRML test sample for measurements with a soft x-ray microscope is formed with two contrast materials, WSi_2 and Si. The BPRML is structured according to a BPR sequence with a total number of elements $N = 2047$, a fundamental thickness of the multilayer $\Delta t \approx 2.8$ nm, and sample width $w = 80 - 100$ nm. It has 1010 layers of the two materials with thicknesses distributed according to the chosen sequence. The thickest layer consists of 11 elementary layers.

The test sample was fabricated in two steps. First, a BPRML with a desired distribution of the layers was deposited on 0.5 mm thick Si (100) substrate of approximately 25 mm × 12.5 mm size. Second, a thin sample cross section was etched out from the multilayer using a focused ion beam (FIB)/SEM sample preparation technique. Finally, the structure quality of the fabricated BPRML test sample was characterized in high resolution TEM measurements.

A. BPR multilayer deposition

The BPRML structures were fabricated with solid-source targets of B-doped Si and hot-pressed WSi2 using modified 3-inch direct-gas injection cathodes[39] in a turbo-pumped rotary deposition system. The target to sample distance was 78 mm, with a process gas pressure of Ar held at a constant 2.3 milliTorr by upstream dual-MFC feedback control. The Ar gas was injected directly behind the cathode dark space shield. The average gas flow through each cathode was ~9 SCCM. Deposition was carried out at a constant power of 170 watts for both sources using Advanced Energy DC sputtering power supplies. Before each layer deposition, the substrate carousel rotated such that the samples are outside the deposition aperture. The power supply initiated plasma and stabilized for 7 seconds. The proper thickness for each individual layer was then produced by raster-scanning the substrate over the apertures by varying both the number of passes over this aperture and the rotational velocity. The apertures were properly shaped to produce an approximately uniform deposition thickness along the direction orthogonal to rotation by a mathematical convolution of the rotational radius, deposition source fingerprint, and uniform coating thickness requirement. This procedure is called profile coating and is described extensively elsewhere.[40] Due to the inherent nature of magnetron deposition growth rate to decay over time, a compensation factor was included during the

growth which adjusts the velocity appropriately, as is used for growth of other types of thick multilayers.[41,42] SEM feedback data from the growth of this structure were incorporated into the deposition process to obtain very accurate BPRML structures.

The deposited BPRML was tested in an x-ray diffraction experiment by measuring the multilayer reflectance as a function of the grazing incidence angle – Fig. 2, black solid line. The measurement was performed with a copper-anode tube source operating at 1.6 kW, and using a multilayer collimating optic and 4-bounce Ge (220) monochromator upstream of the sample. The beam size impinging on the sample is fixed with slits at approximately 50 μm by 8 mm. A semiconductor strip detector integrated the specular reflectance to produce the diffraction data with one point taken every 0.001 degrees theta. Beam intensity was determined by aiming the detector directly at the source with the sample removed and recording for 10 seconds. The initially low reflectance below 0.4 degrees is due to incomplete sample illumination by the incident beam. Data fitting was performed using IMD software[43] by importing the design BPRML layer data file (with every layer thickness proportionally reduced by 8%), incorporating a 0.25 nm interlayer roughness, and a top silicon oxidation layer of 1.5 nm. Although an x-ray reflectance measurement is not the proper way to fully characterize a multilayer structure such as this, a comparison of the measured pattern with a result of corresponding simulation (red dashed line in Fig. 2) provides a quick and reliable check of the structure of the top-surface layers.[41,42] Good agreement between the measured and simulated diffraction patterns suggests that the top-surface layers correspond to the desired structure given by the chosen binary sequence. From the simulations,[43] the fundamental thickness of the BPR multilayer was found to be 2.76 nm.

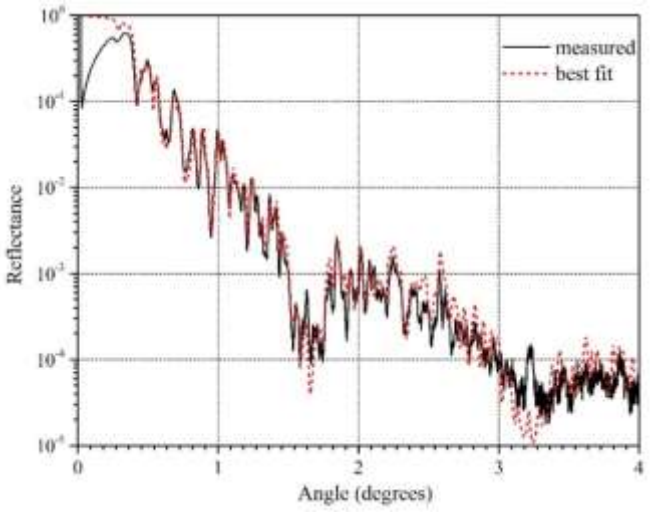

FIG. 2. Dependence of BPRML reflectance on grazing incidence angle. The measurement (black solid line) and simulation (red dashed line) were performed with 8.048 keV x-rays ($CuK_{\alpha 1}$). Good agreement between the measured and simulated diffraction patterns suggests that the top-surface layers correspond to the desired structure given by the sequence used. The value of the fundamental thickness of the multilayer found from the simulations is 2.76 nm.

B. FIB/SEM sample preparation

A BPRML test sample was etched out from the multilayer using a FIB/SEM technique. A Dual Beam FIB/SEM instrument (Helios NanoLab,™ FEI Company) available at Evans Analytical Group (EAG), LLC[44,45] was used. The instrument integrates imaging capabilities of a field emission SEM and the capability for preparation of a precise thin sample cross section using the FIB technique.[46] In order to avoid rounding of the top surface edge of the etched piece in the course of FIB etching, the surface of the multilayer was first coated with a 1.5 μm thick layer of Pt.

In the course of sample preparation, a small (approximately 10 μm × 15 μm × 2 μm) piece was completely detached from the multilayer and Pt-ion-beam welded to a pin on a standard copper 5-post lift-out grid – Fig. 3.

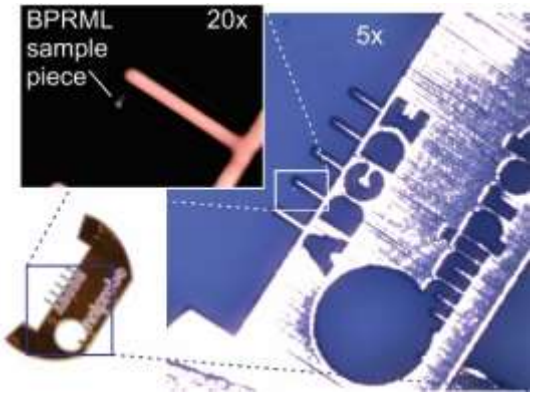

FIG. 3. Multilayer sample piece attached to the B pin of a standard copper 5-post lift-out grid. The images were obtained with an optical microscope equipped with 5× and 20× objectives.

Figures 4 shows a high resolution photomicrograph of the BPRML test sample attached to a pin of the lift-out grid. The 1.5 μm thick, protection layer of Pt is seen as a lighter top layer of the multilayer piece. The darker bottom layer of approximately 5 μm thick is a piece of the Si substrate.

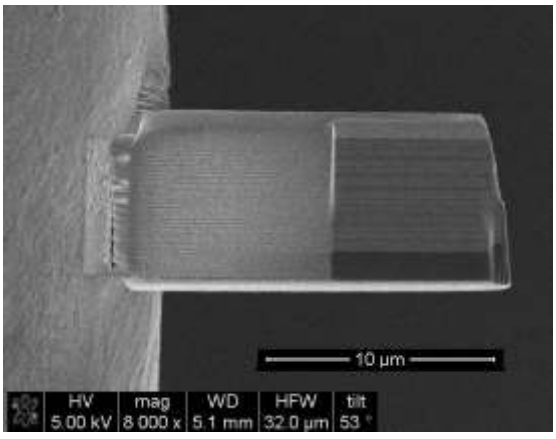

FIG. 4. Photomicrograph of the multilayer piece attached to a pin of standard copper 5-post lift-out grid (see Fig. 3). The part of the ML piece processed with 'super-polishing' at extremely low FIB current and voltage is at the free end of the sample piece. The target sample width (in the direction perpendicular to the plane of the picture) is approximately 80 nm.

Finally, in order to decrease the test sample piece thickness to the desired 60-100 nm and provide a uniform thickness, both sides of the ML piece at its free end were processed with fine FIB polishing ('super polishing') at extremely low ion beam current. An SEM image of the test sample taken just before the last cycle of final fine FIB polishing of the sample's front and back surfaces is shown in Fig. 5a. Because SEM imaging often contaminates the sample surface, there is no SEM image taken after the last cycle of the FIB polishing.

C. TEM characterization of the BPRML test sample

When the sample preparation was completed, the FIB/SEM vacuum chamber was vented and the lift-out grid with the sample was moved for TEM characterization, also performed at EAG, LLC. The structure of the multilayer of the BPRML test sample was investigated with a Tecnai^{TM} TEM instrument (FEI, Co.), available at the EAG, LLC.

In order to get the entire cross section of the sample, a low resolution TEM measurement of the BPRML was made at relatively low electron energy of 2.3 keV – Fig. 5b. The resolution of the TEM image is noticeably higher than that of the SEM image. The contrast variation from top to bottom of the image is probably due to the variation of the sample thickness. The overall height of the BPR multilayer as measured with the TEM is 5.80 μm. That provides an estimation of the multilayer fundamental thickness of 2.83 nm. This value is in excellent agreement with the fundamental thickness of 2.76 nm measured in the diffraction experiment (Fig. 2). The average value of 2.80 nm is used for the simulation discussed below.

In order to get a reasonably high resolution TEM image of the entire cross-section of the BPRML sample, an analytical stitching procedure was developed and applied to a serious of the overlapped images, preliminarily detrended with a plane surface. For stitching the images, we use graphic design software CorelDraw that allows visually pre-aligning and positioning the images with required precision. However, while graphic design software makes the process of image stitching relatively simple, there are some caveats. Because the software employs a highly sophisticated algorithms for treating images, this can lead to a significant distortion of the data stored in the images used for stitching. Newer the less, the usage of the stitching for illustration purposes, like the one here, is perfectly acceptable.

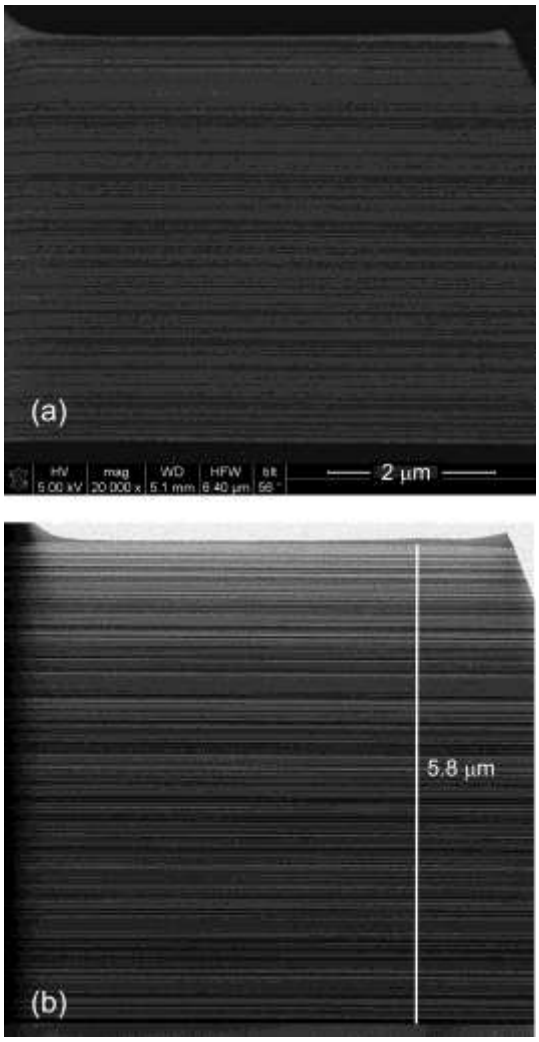

FIG. 5. (a) SEM image of the BPRML test sample piece taken just before the last cycle of the FIB polishing. (b) A low magnification TEM image of the BPRML sample piece, processed with the final fine FIB polishing.

Figure 6 presents a TEM image of a cross section of the BPRML sample obtained by analytically stitching the eight images measured at an electron energy of 17.5 keV. The left-hand side of the stitched image in Fig. 6 corresponds to the top of the sample in the previous figures. The top Pt layer and the bottom Si substrate residual are cut out.

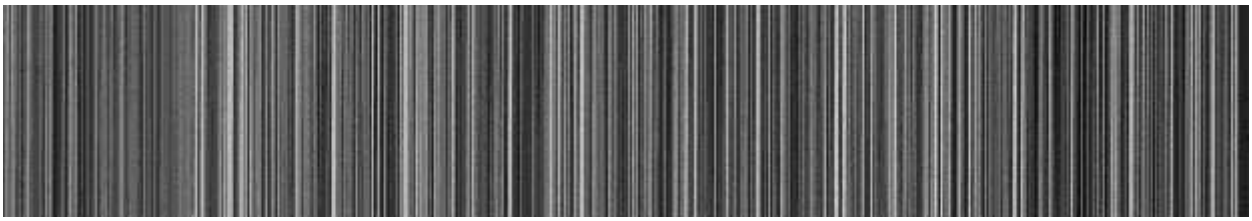

FIG. 6. TEM image of a cross section of the BPRML sample obtained by analytically stitching the eight images measured at the electron energy of 17.5 keV. The left-hand side of the image corresponds to the top of the sample in Fig. 5.

The superior quality of the deposited multilayer was confirmed in high resolution TEM measurements[47] with the fabricated sample, performed at electron energy of 255 keV– Fig. 7. In this case, the instrumental resolution of about 2Å allows observation of the interlayers of the coating. The measurements were performed over areas of the BPRML sample approximately uniformly distributed along the vertical direction of the sample cross-section, as is depicted in the inset (a). The inset corresponds to the low resolution measurement of the entire cross-section shown in Fig. 5b.

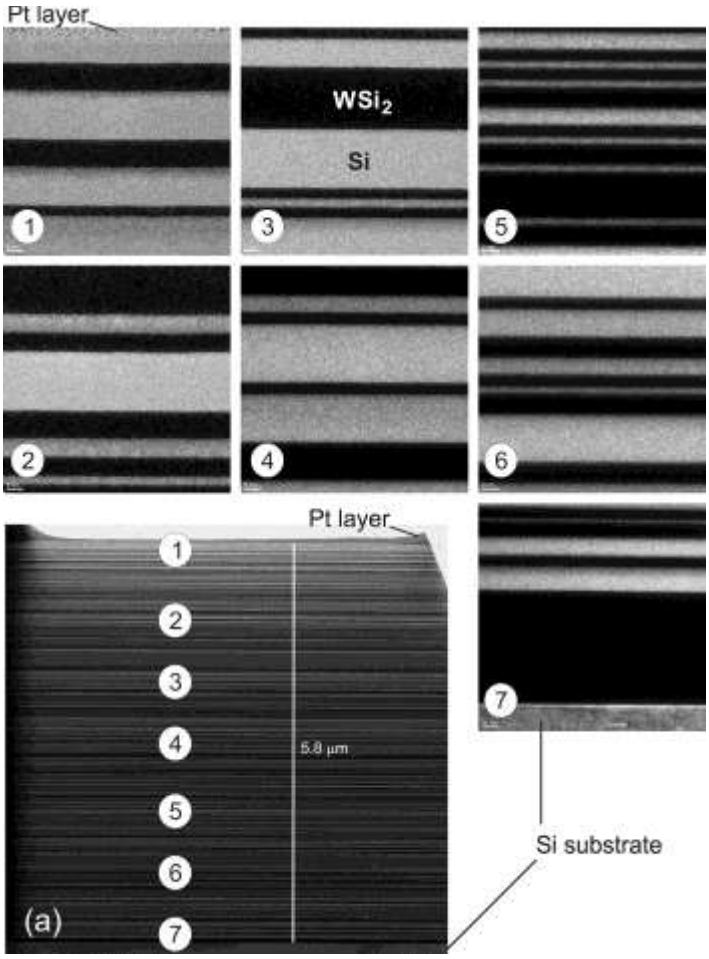

FIG. 7. High resolution (255 keV electron energy) TEM measurements with the BPRML sample. The distribution of the measured areas along the vertical direction of the sample cross-section is approximately depicted with the inset (a) that corresponds to Fig. 5b. The measurements confirm the high quality of the BPRML test sample.

The major conclusions from the TEM measurements are that the BPR multilayer has extremely uniform thickness of the layers and that the separation between the layers of different materials is very sharp with a transition thickness much smaller than the multilayer fundamental thickness. These small fabrication imperfections have little to no effect on the sample's inherent PSD distribution over its entire spatial frequency range (see discussion in Ref.[16]).

III. MTF CHARACTERIZATION OF THE A SOFT X-RAY MICROSCOPE

The unique features of soft x-ray microscopy have found numerous applications in life sciences,[48] materials science (particularly, magnetic imaging[49]), and environmental science.[50] Using soft x-rays in microscopic imaging provides inherent elemental specificity, chemical and magnetic sensitivity, high spatial resolution down to the nanometer length scale as well as time resolved studies of sub-nanosecond dynamical processes harnessing the inherent pulsed time structure of soft x-ray sources, e.g. at synchrotron facilities. The optical design of the full field transmission soft x-ray microscope XM-1 at the ALS beamline 6.1.2 (see Ref.[38] and references therein) is similar to a conventional visual light microscope and follows the concept of the first full-field soft x-ray microscope described in Ref.[51] As optical lenses do not work for x-rays, soft x-ray microscopes in general utilize Fresnel zone plates as x-ray optical elements. At XM-1 there is a large condenser zone plate and a smaller micro zone plate used as an objective lens. Although, state-of-the-art FZPs have demonstrated a better than 10 nm spatial resolution in test patterns,[52] the current nominal spatial resolution of XM-1 is approximately 25 nm.

For performance tests of the Fresnel zone plate optics a simple, fast and reliable resolution test tool is highly desirable. The goal of the x-ray microscope experiments, discussed in this paper, is to develop and demonstrate a method based on BPRML test samples for quantitative characterization of the instrumental MTF over its entire spatial frequency range.

A. TXM measurement with the BPRML test sample and data processing

Figure 8a shows an image of the BPRML test sample recorded with the XM-1 x-ray microscope equipped with an ‘objective’ zone plate with an outermost zone width of 25 nm, which provides about 25 nm spatial resolution. The image was recorded at 707 eV photon energy with an exposure time of 1.6 sec. A typical field of view with a diameter of about 0.01 mm is recorded with a detector CCD camera (Fig. 8) with 2048 × 2048 pixels corresponding to an equivalent pixel size of 4.9 nm × 4.9 nm.

The BPR structure of the sample is well resolved with contrast and resolution that appear to be very similar to that of the SEM and TEM in Fig. 5. The low spatial frequency brightness variation across the multilayer is possibly due to the non-uniformity of the sample width.

In order to extract information about the microscope's MTF and resolution, images like the one shown in Fig. 8a are first rotated to make the analysis easier, cropped in order to remove the image area outside the multilayer, and detrended with a quartic surface in order to make the mean variation of intensity values equal to zero.

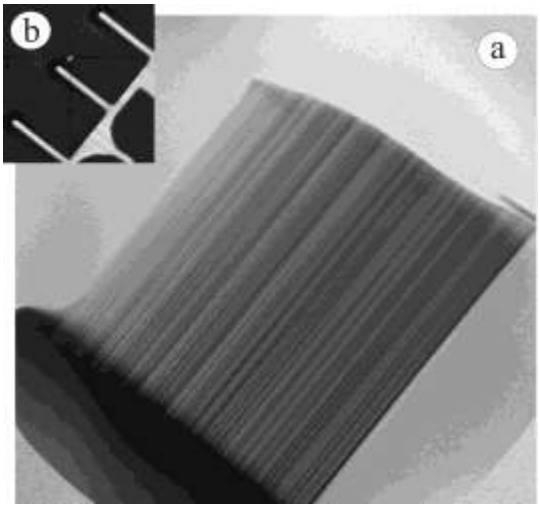

FIG. 8. (a) Image of the BPRML test sample recorded with the ALS XM-1 x-ray microscope equipped with an 'objective' zone plate with outermost zone width 25 nm. The measurement was performed at 707 eV photon energy. The whole area of the detector CCD camera is covered by 2048 × 2048 pixels with an equivalent size of 4.9 nm × 4.9 nm. (b) Image of the multilayer sample piece attached to the B pin of a standard copper 5-post lift-out grid obtained with a visual light microscope at the ALS beamline 6.1.2 used for pre-alignment of the sample.

Second, the measured image is matched to the theoretical one built from the BPR sequence that was used to specify the BPR multilayer deposition. The initial matching is performed by determining the mutual position of the whole image that corresponds to the maximum cross-correlation of the images. Here, the images are scaled according to the nominal effective pixel size of 4.9 nm of the measured image and the measured fundamental thickness of the test sample of 2.8 nm. After initial matching, the matching is repeated for a series of sub-areas of the theoretical image and the dependence of the best matched positions of the corresponding sub-areas in the measured image as a function of the position of the subareas of the theoretical image is plotted. In order to find a correction factor for precision rescaling of the images, the data are fitted with a linear polynomial. The correction factor, found to be 1.0087±0.0005, was applied to rescale the theoretical image. Note that the high accuracy of the diffraction and TEM measurements of the fundamental thickness of the BPRML test sample can also be used for precise lateral calibration of the x-ray microscope.

Figure 9 depicts the result of the matching process as applied to the XM-1 image of the BPRML sample placed in the microscope at lateral position $z = -785\,\mu\text{m}$ (in the coordinate system of the microscope).

The matched theoretical image in Fig. 9 is resampled to the pixel size of the measured image. In order to increase the accuracy of the resampling, the theoretical image is first oversampled by splitting of each original pixel to 10 sub-pixels. Finally, the oversampled image is converted to the pixel grid of the measured image by averaging the intensities of the sub-pixels enveloped with a particular pixel of the measured grid.

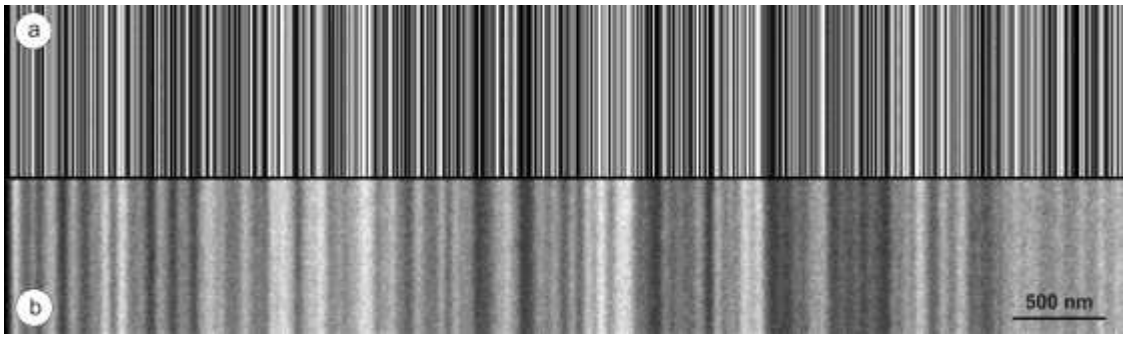

FIG. 9. The matched images: (a) the rescaled computer-generated ideal theoretical image and (b) the images measured with the soft x-ray microscope XM-1 at the ALS BL 6.1.2.

Third, a discrete Fourier transformation is applied to the experimental image and 2D PSD distributions are calculated. After that the 2D distributions are convolved into 1D PSD spectra for the horizontal and vertical directions, 1D PSD_X and 1D PSD_Y, respectively – Fig. 10. At lower spatial frequencies, the 1D PSD_X spectrum is flat, reproducing the white-noise-like character of the BPRML test sample under measurement. The sharp roll-off of the 1D PSD_X at the spatial frequency of around 15 μm^{-1} is a signature of a finite resolution of the instrument.

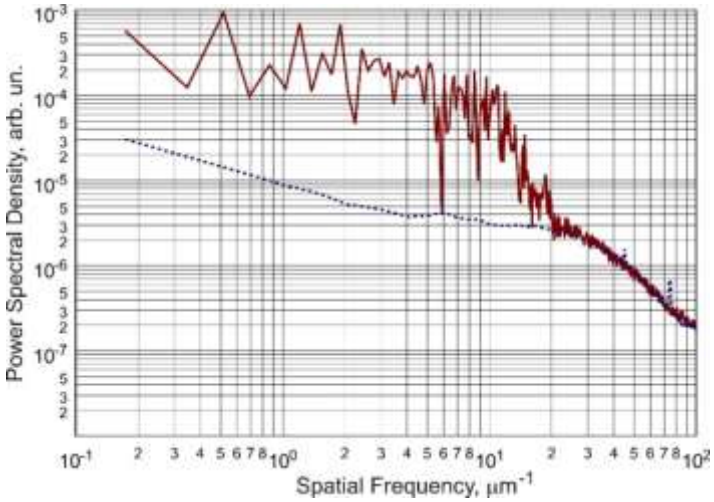

FIG. 10. 1D PSD spectra obtained by integration of the 2D PSD of the XM-1 image of the 2.8-nm BPRML test sample, shown in Fig. 9b: the horizontal (solid red line) and the vertical (dashed blue line) 1D PSDs.

The PSD spectrum in the vertical direction, 1D PSD_Y, is significantly different. Because of the sample structure, the flat pattern is absent. The 1D PSD_Y spectrum is mostly due to the instrumental noise, artifacts of the measurement (e.g., instrumental aberrations), and possible imperfections of the sample itself (e.g., a variation of the sample width). One can expect that the contributions of these sources to the 1D PSD_X and 1D PSD_Y are the same. Indeed, at the spatial frequencies higher than the resolution cut-off, where the contribution of the BPRML structure is negligible and, therefore, the instrumental noise and aberrations are dominant, the horizontal and the vertical PSDs are almost identical. This allows us to use the 1D PSD_Y as a measure of the background in the 1D PSD_X.

Figure 11 shows the difference between the PSD spectra in the horizontal and in the vertical direction. The subtraction of the background provides the PSD distribution that, if normalized to the unit level at the lower spatial frequencies, can be thought of as a measure of the microscope MTF squared. The cut-off frequency of approximately 20 μm,$^{-1}$ where the PSD from the sample becomes negligibly small, is the resolution limit of the microscope.

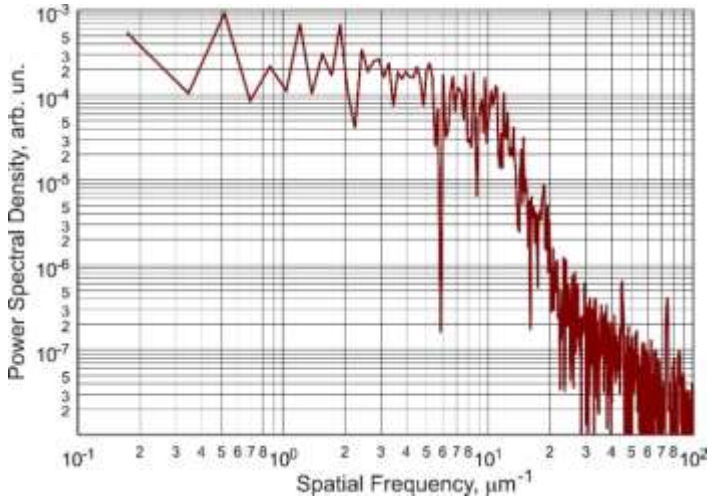

FIG. 11. 1D PSD spectrum obtained by subtraction of the 1D PSD_Y from 1D PSD_X shown in Fig. 10. If normalized to the unit level at the lower spatial frequencies, the spectrum can be thought of as a measure of the microscope MTF^2.

Finally, the measured PSD spectrum is compared with a theoretical PSD spectrum inherent to the BPRML test sample used (Fig. 9a), resampled to correspond to the measurements with an ideal x-ray microscope of which resolution is limited only by the effective pixel size of the detector. The theoretical PSD_X is shown in Fig. 12 together with the measured one.

The strong correlation of the measured and the theoretical PSD spectra at the spatial frequencies up to approximately 10 μm^{-1} is clearly seen in Fig. 12. However, the behavior of the spectra near the roll-offs is significantly different. This is due to the MTF of the x-ray microscope.

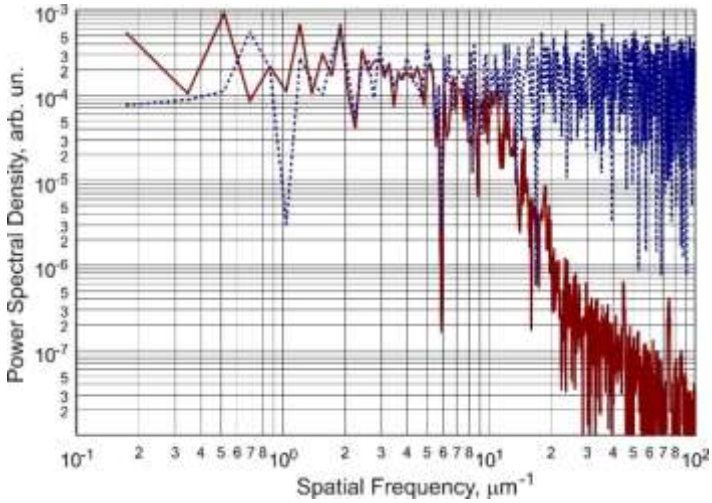

FIG. 12. Theoretical 1D PSD_X spectrum, inherent to the BPRML test sample used (Fig. 9a), resampled to correspond to the measurements with an ideal x-ray microscope of which resolution is limited only by the effective pixel size of the detector (dashed blue line); and the measured 1D PSD_X spectrum, shown also in Fig. 11 (solid red line). The instrumental MTF^2 appears as the difference of the spectra near the higher spatial frequency roll-off of the measured PSD.

B. Determining the MTF

Here, we approximate the microscope's MTF with a squared Gaussian function of the form:

$$MTF^2(f) = exp\left(-2\frac{f^2}{\sigma_f^2}\right), \tag{2}$$

where σ^2 is the dispersion of the Gaussian MTF. Such an approximation is very natural if one takes into account that in the spatial domain, the resolution (point spread function, PSF) of the microscope relates to many uncorrelated perturbations of different form:

$$PSF(x) \equiv Fourier^{-1}\left(MTF\right) = Fourier^{-1}\left(exp\left(-\frac{f^2}{\sigma_f^2}\right)\right) = 2^{-1/2}\sigma_x^{-1}exp\left(-\frac{1}{4}\frac{\rho^2}{\sigma_x^2}\right), \tag{3}$$

where $\sigma_x = \sigma_f^{-1}$ and $\rho = \pi r$, where r is the radial coordinate of the beam spot. Note that the Gaussian-like PSF in the form of Eq. (3) is a good approximation of the diffraction limited PSF given with the Airy function.

The validity of this analytical parametrization of the microscope MTF is illustrated with Fig. 13, where the Gaussian MTF, given by Eq. (2) with $\sigma_f = 11\,\mu m,^{-1}$ is applied to the theoretical 1D PSD_X (dashed blue line).

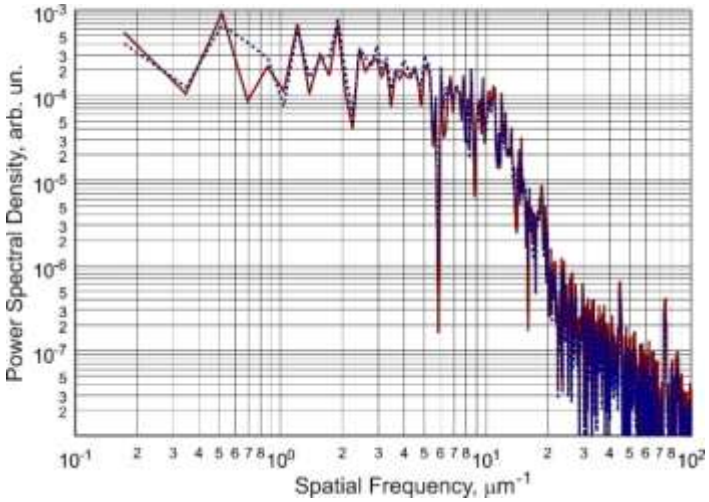

FIG. 13. Result of application of the Gaussian MTF described by Eq. (2) with $\sigma = 11$ μm^{-1} to the theoretical 1D PSD$_X$ (dashed blue line) and 1D PSD$_X$ distribution of the 2.8-nm BPRML test sample measured with the soft x-ray microscope XM-1 (solid red line).

We also add to the theoretical PSD a fractal-like residual noise, described with a function

$$Offset = A / f^{p} \tag{4}$$

that best fit the high spatial frequency tail of the measured 1D PSD$_Y$ in Fig. 10.

The result of the application of the Gaussian MTF to the theoretical PSD very well matches the 1D PSD$_X$ measured with XM-1 microscope (solid red line in Fig. 13), even reproducing the fine variation of the PSD over almost the entire spatial frequency bandwidth of the microscope. The high special frequency cut-off at $f_{CUT-OFF} \approx 2\sigma_f \approx 22$ μm^{-1} corresponds to the microscope lateral resolution limit of approximately 45 nm.

C. Dependence of XM-1 microscope's MTF on the lateral position of the test sample

The data processing procedure, discussed above, can also be applied to the XM-1 images of the BPRML sample placed in the microscope at different lateral positions. Such an image, obtained at $z = -790$ μm (5 μm shift from the previous position) is depicted in Fig. 14.

FIG. 14. The matched images: (a) the rescaled computer-generated ideal theoretical image and (b) the XM-1 images measured with the BPRML sample placed in the microscope at the lateral positions of $z = -790$ μm.

Figure 15 presents the 1D PSD_X spectrum of the image in Fig. 11b. For comparison, the 1D PSD spectrum measured with the sample placed at $z = -785$ µm is also shown. The lateral shift of the sample by 5 µm clearly leads to degradation of the microscope's resolution.

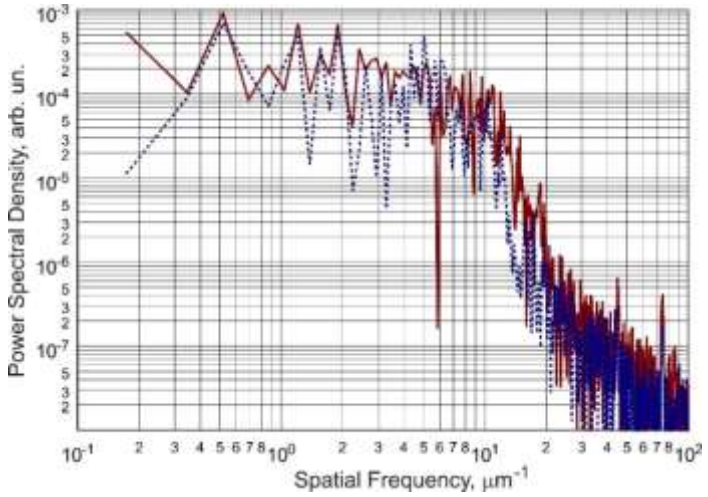

FIG. 15. 1D PSD spectra of the XM-1 image of the 2.8-nm test sample placed at $z = -790$ µm (dashed blue line), obtained by subtraction of the corresponding 1D PSD_Y from 1D PSD_X; and the 1D PSD spectrum measured with the sample at $z = -785$ µm (red solid line).

The best fit of the PSD spectrum corresponding to $z = -790$ µm with the theoretical PSD spectrum filtered with the MTF in the form of Eq. (2) is obtained with $\sigma_f \approx 8\,\mu m^{-1}$ – see Fig. 16.

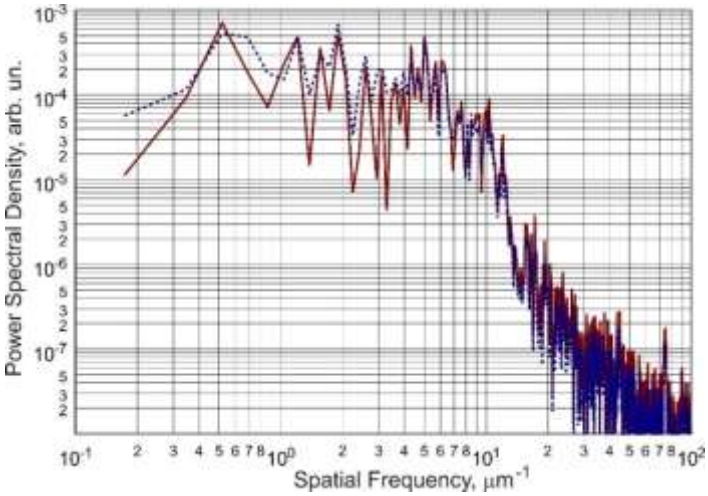

FIG. 16. Result of application of the Gaussian MTF described by Eq. (1) with $\sigma = 8\,\mu m^{-1}$ to the theoretical 1D PSD_X (dashed blue line) and 1D PSD_X distribution of the 3-nm BPRML test sample measured with the soft x-ray microscope XM-1 (solid red line) placed at lateral position $z = -790$ µm.

In order to understand the sensitivity of the MTF measurement procedure, described above, to the lateral position of the sample (defocus), an analytical parameterization of the Gaussian MTFs given by Eq. (2) was applied

to the BPRML sample images recorded with the XM-1 microscope when the sample position was changed in increments of 1 μm within the range of $z = -785\,\mu m$ and $z = -790\,\mu m$. Figure 17 summarizes the results of the measurements as sample position dependence of the spatial frequency cut-off $f_{CUT-OFF}$, defined as $f_{CUT-OFF} \equiv 2\sigma_f$.

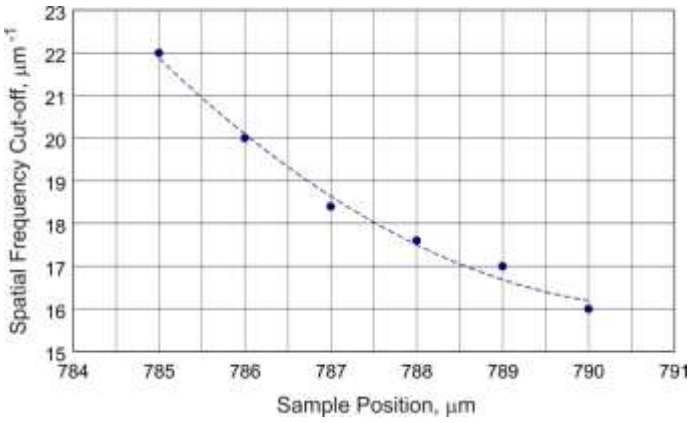

FIG. 17. Dependence of the spatial frequency cut-off $f_{CUT-OFF}$, defined as $f_{CUT-OFF} \equiv 2\,\sigma_f$ on the test sample lateral position. The second polynomial fit is shown just for guidance of the data points.

The data in Figs. 16 and 17 demonstrate that beyond providing a direct measurement of the microscope's MTF, tests with the BPRML sample can be used to fine tune the instrument's focal distance. In the case of the soft x-ray microscope XM-1 at the ALS BL 6.1.2, the sensitivity of the MTF to the defocus is adequate for optimizing the focal distance with sub-micron accuracy.

VI. CONCLUSIONS

A binary pseudo-random multilayer test sample with fundamental layer thickness of 2.8 nm and a total useful area of about 6 μm × 6 μm has been developed using FIB/SEM sample development techniques. The sample was comprehensively characterized with SEM and TEM measurements at different instrumental resolutions. The measurements have confirmed the high quality of the BPR multilayer deposited at NSLS-II. The sharp image contrast between the WSi_2 and Si layers has been demonstrated by super high resolution measurements by scanning TEM.

In this work, this sample was used to characterize the MTF of a soft x-ray transmission microscope. The performed measurements have allowed us to precisely measure the spatial frequency cut-off associated with the limited resolution of the instrument. A procedure to extract the information about the microscope's MTF and resolution from the obtained images has been described.

We have also demonstrated that beyond providing a direct measurement of the microscope's MTF, tests with the BPRML sample can be used to fine tune the instrument's focal distance. In the case of the microscope XM-1, the sensitivity of the MTF to the defocus is adequate for optimizing the focal distance with sub-micron accuracy.

Our investigations confirm the potential of a new method based on BPRML test samples for quantitative characterization of the instrumental MTF over its entire spatial frequency range. The high frequency cut-off of the measured MTF provides a measure of the instrumental spatial resolution. By varying the microscope parameters, such as focal distance, one can optimize the resolution via maximization of the MTF cut-off frequency.

ACKNOWLEDGMENTS

The authors are grateful to David Susnitzky, Mark Izquierdo, and Udit Sharma for the FIB/SEM sample preparation and the TEM measurements. This work was supported in part by the UC Office of the President, Proof of Concept Grant ID No. 268826 and by the U.S. Department of Energy Office of Science, Office of Basic Energy Sciences Energy Small Business Technology Transfer (STTR) program under Award Numbers DE-SC0011352. The Advanced Light Source and the Molecular Foundry are supported by the Director, Office of Science, Office of Basic Energy Sciences, Material Science Division, of the U.S. Department of Energy under Contract No. DE-AC02-05CH11231 at Lawrence Berkeley National Laboratory. Research at Brookhaven National Laboratory is sponsored by the U.S. Department of Energy under Contract No. DE-AC02-98CH10886. Research at Argonne National Laboratory is sponsored by the U.S. Department of Energy under Contract No. DE-AC02-06CH11357. P. F acknowledges support by the Director, Office of Science, Office of Basic Energy Sciences, Materials Sciences and Engineering Division, of the U.S. Department of Energy under Contract No. DE-AC02-05-CH11231 and the Leading Foreign Research Institute Recruitment Program (Grant No. 2012K1A4A3053565) through the National Research Foundation of Korea (NRF) funded by the Ministry of Education, Science and Technology (MEST).

DISCLAIMER

This document was prepared as an account of work sponsored by the United States Government. While this document is believed to contain correct information, neither the United States Government nor any agency thereof, nor The Regents of the University of California, nor any of their employees, makes any warranty, express or implied, or assumes any legal responsibility for the accuracy, completeness, or usefulness of any information, apparatus, product, or process disclosed, or represents that its use would not infringe privately owned rights. Reference herein to any specific commercial product, process, or service by its trade name, trademark,

manufacturer, or otherwise, does not necessarily constitute or imply its endorsement, recommendation, or favor by the United States Government or any agency thereof, or The Regents of the University of California. The views and opinions of authors expressed herein do not necessarily state or reflect those of the United States Government or any agency thereof or The Regents of the University of California.

REFERENCES

[1]R. N. Bracewell, The Fourier Transform and Its Applications, McGraw-Hill Publishing Company, New York (1986).

[2]G. M. Jenkins and D. G. Watts, Spectral analysis and its applications, Emerson-Adams Press, Boca Raton (2000).

[3]J. W. Goodman, Fourier Optics, 3rd Ed., Roberts and Co., Englewood (2005).

[4]J. M. Elson, J. M. Bennett, "Calculation of the power spectral density from surface profile data," Appl. Opt. 34(1), 201 (2001).

[5]V. V. Yashchuk, S. C. Irick, E. M. Gullikson, M. R. Howells, A. A. MacDowell, W. R. McKinney, F. Salmassi, T. Warwick, "Cross-check of different techniques for two dimensional power spectral density measurements of x-ray optics," Proc. SPIE 5921, 59210G (2005).

[6]G. D. Boreman, Modulation Transfer Function in Optical and Electro-optical Systems, SPIE Press, Bellingham, Washington (2001).

[7]M. Marchywka, D. G. Socker, "Modulation transfer function measurement technique for small pixel detectors," Appl. Opt. 31(34), 7198 (1992).

[8]G. D. Boreman, and S. Yang, "Modulation transfer function measurement using three- and four-bar targets," Appl. Opt. 34(34), 8050 (1995).

[9]E. Levy, D. Peles, M. Opher-Lipson, and S. G. Lipson, "Modulation transfer function of a lens measured with a random target method," Appl. Opt. 38(4), 679 (1999).

[10]J. Chu, Q. Wang, J. P. Lehan, G. Gao, and U. Griesmann, "Spatially resolved height response of phase-shifting interferometers measured using a patterned mirror with varying spatial frequency," Opt. Eng. 49(9), 095601 (2010).

[11]V. V. Yashchuk, W. R. McKinney, and P. Z. Takacs, "Test Surfaces Useful For Calibration Of Surface Profilometers," U.S. patent application 20100037674 (18 February 2010); U.S. patent 8,616,044 (31 December 2013).

[12]V. V. Yashchuk, W. R. McKinney, and P. Z. Takacs, "Binary Pseudorandom Grating Standard for Calibration of Surface Profilometers," Proc. SPIE 6704, 670408 (2007); Opt. Eng. 47(7), 073602 (2008).

[13]S. K. Barber, P. Soldate, E. D. Anderson, R. Cambie, W. R. McKinney, P. Z. Takacs, D. L. Voronov, and V. V. Yashchuk, "Development of Pseudo-random Binary Gratings and Arrays for Calibration of Surface Profile Metrology Tools," J. Vac. Sci. and Tech. B 27(6), 3213 (2009).

[14]S. K. Barber, E. D. Anderson, R. Cambie, W. R. McKinney, P. Z. Takacs, J. C. Stover, D. L. Voronov, and V. V. Yashchuk, "Binary Pseudo-Random Gratings and Arrays for Calibration of Modulation Transfer Function of Surface Profilometers," Nucl. Instr. and Meth. A 616, 172 (2010).

[15]S. K. Barber, P. Soldate, E. D. Anderson, R. Cambie, S. Marchesini, W. R. McKinney, P. Z. Takacs, D. L. Voronov, V. V. Yashchuk, "Binary Pseudo-random Gratings and Arrays for Calibration of the Modulation Transfer Function of Surface Profilometers: Recent Developments," Proc. SPIE 7448, 744802-1-12 (2009).

[16]S. K. Barber, E. Anderson, R. Cambie, S. Marchesini, W. R. McKinney, P. Z. Takacs, D. L. Voronov, V. V. Yashchuk, "Stability of modulation transfer function calibration of surface profilometers using binary pseudo-random gratings and arrays with non-ideal groove shapes," Opt. Eng. 49(5), 053606 (2010).

[17]V. V. Yashchuk, E. H. Anderson, S. K. Barber, N. Bouet, R. Cambie, R. Conley, W. R. McKinney, P. Z. Takacs, D. L. Voronov, "Calibration of the modulation transfer function of surface profilometers with binary pseudo-random test standards: expanding the application range to Fizeau interferometers and electron microscopes," Opt. Eng. 50(9), 093604 (2011).

[18]V. V. Yashchuk, R. Conley, E. H. Anderson, S. K. Barber, N. Bouet, W. R. McKinney, P. Z. Takacs, D. L. Voronov, Characterization of electron microscopes with binary pseudo-random multilayer test samples, Nucl. Instr. and Meth. A 649(1), 150 (2011).

[19]P. H. Bardell, W. H. McAnney, J. Savir, Built-in test for VLSI pseudorandom techniques, John Wiley and Sons, Inc., New York (1987).

[20]A. Busboom, H. Elders-Boll, H. D. Schotten, "Uniformly Redundant Arrays," Experimental Astronomy: Astrophysical Instrumentation and Methods 8, 97 (1998).

[21]B. Sclar, Digital Communications: Fundamentals and Applications, 2nd Ed., Prentice Hall (2001).

[22]T. Etzon, "Construction for perfect maps and pseudo-random arrays," IEEE Trans. on Information Theory 34(5), 1308 (1988).

[23]D. D. Koleske, and S. J. Sibener, “Generation of pseudo-random sequence for use in cross-correlation modulation,” Rev. Sci. Instrum. 63(8), 3852 (1992).

[24]A. Mitra, "On pseudo-random and orthogonal binary spreading sequences," International Journal of Information and Communication Engineering 4(6), 447 (2008).

[25]W.T. Chu, "Impulse-Response and Reverberation-Decay Measurements Made by Using a Periodic Pseudorandom Sequence, " Appl. Acoustics 29, 193 (1990).

[26]T.E. Stern, A. Blaquiere, J. Valat, "Reactivity Measurement Using Pseudo-Random Source Excitation," J. Nucl. Energy Pt. A and B 16(11-12), 499 (1962).

[27]J. Gordon, N. Kroo, G. Orban, L. Pal, P. Pellionisz, F. Szlavik, I. Vizi, "Correlation Type Time-of-Flight Spectrometer with Magnetically Pulsed Polarized Neutrons," Phys. Lett. A 26(3), 122 (1968).

[28]K. Skold, "A Mechanical Correlation Chopper for Thermal Neutron Spectroscopy," Nucl. Instr. and Meth. 63, 114 (1968).

[29]A. Virjo, "Statistical Analysis of Cross-Correlation Chopper for Time-of-Flight Measurements," Nucl. Instr. and Meth. 63, 351 (1968).

[30]A. Virjo, "The Fourier method in Slow neutron time-of-flight Spectrometry with a Pseudo-Random Input Signal," Nucl. Instr. and Meth. 73, 189 (1969).

[31]A. Virjo, "Slow Neutron Time-of-Flight Spectrometry with a Pseudo-Random Input Signal," Nucl. Instr. and Meth. 75(1), 77 (1969).

[32]V. L. Hirschy, and J. P. Aldridge, "A Cross Correlation Chopper for Molecular Beam Modulation," Rev. Sci. Instrum. 42(3), 381 (1971).

[33]G. Comsa, R. David, and B. J. Schumacher, "Magnetically suspended cross-correlation chopper in molecular beam-surface experiments," Rev. Sci. Instrum. 52(6), 789 (1981).

[34]V. V. Yashchuk, B. N. Ashkinadzi, M. N. Groshev, V. F. Ezhov, T. A. Isaev, V. A. Knyazkov, G. B. Krygin, V. L. Ryabov, "Cross-Correlation Time-of-Flight Spectrometer of Molecular Beams," Instrum. and Exper. Techniques 40(4), 501 (1997).

[35]S. M. Kay, Modern Spectral Estimation: Theory and Application, Prentice Hall, Englewood Cliffs (1988).

[36]E. E. Fenimore, and T. M. Cannon, "Coded aperture imaging with uniformly redundant arrays," Appl. Opt. 17(3), 337 (1978).

[37]E. Caroli, J. B. Stephen, G. Di Cocco, L. Natalucci, A. Spizzichino, "Coded aperture imaging in x- and gamma-ray astronomy," Space Science Reviews 45, 349 (1987).

[38]P. Fischer, D.-H. Kim, W. Chao, J. A. Liddle, E. H. Anderson, and D. T. Attwood, "Soft X-Ray Microscopy of nanomagnetism," Materials Today 9(1-2), 26 (2006).

[39]Materials Science, Inc., http://www.msi-pse.com/Polaris.htm.

[40]C. Liu, L. Assoufid, R. Conley, A. T. Macrander, G. E. Ice, and J. Z. Tischler, "Profile coating and its application for Kirkpatrick-Baez mirrors," Opt. Eng. 42(12), 3622-3628 (2003).

[41]R. Conley, C. Liu, J. Qian, C. M. Kewish, A. T. Macrander, H.Yan, H. C. Kang, J. Maser, and G. B. Stephenson, "Wedged multilayer Laue lens," Rev. Sci. Instrum. 79, 053104 (2008).

[42]R. Conley, C. Liu, C.M. Kewish, A.T. Macrander, C. Morawe, "Multilayer Growth in the APS Rotary Deposition System," Proc. SPIE 6704, 670505 (2007).

[43]D. L. Windt, "IMD—Software for modeling the optical properties of multilayer films," Computers in physics, Am. Inst. Phys. 12(4), 360 (1998).

[44]L. A. Giannuzzi, F.A. Stevie, Introduction to Focused Ion Beams: Instrumentation, Theory, Techniques, and Practice (Springer, New York, 2005).

[45]Evans Analytical Group, LLC, http://www.eaglabs.com.

[46]Evans Analytical Group, LLC, Analytical Solutions for BioTechnology, EAG Bio Technology Application Note BN 1333, ver. 2.0 (2007); http://www.eaglabs.com/files/appnotes/BN1333.pdf

[47]Evans Analytical Group, LLC, EAGLABSSM Transmission Electron Microscopy (TEM) and Scanning Transmission Electron Microscopy (STEM) Services, EAG Technique Note TN 110, ver. 1.0 (2008); http://www.eaglabs.com/files/techniquenote/TN110.pdf

[48]M. A. Le Gros, C. G. Knoechel, M. Uchida, D. Y. Parkinson, G. McDermott, C. A. Larabell, "Visualizing sub-cellular organization using soft x-ray tomography," Comprehensive Biophysics 2, 90 (2012).

[49]P. Fischer and C.S. Fadley, "Probing nanoscale behavior of magnetic materials with soft X-ray spectro-microscopy," Nanotechnology Reviews 1, 5-15 (2012).

[50]J. Thieme, I. McNulty, D. Paterson, S. Vogt: X-ray Spectromicroscopy - A Tool for Environmental Sciences. Environmental Science & Technology, 6885-6887 (2007).

[51]G. Schmahl, D. Rudolph, B. Niemann, and O. Christ, "Zone-plate X-ray microscopy," *Quarterly Reviews of Biophysics* 13(3), 297 (1980).

[52]W. Chao, P. Fischer, T. Tyliszczak, S. Rekawa, E. Anderson, P. Naulleau, "Real Space Soft X-ray Imaging at 10 nm Spatial Resolution," Optics Express 20(9) 9777 (2012).

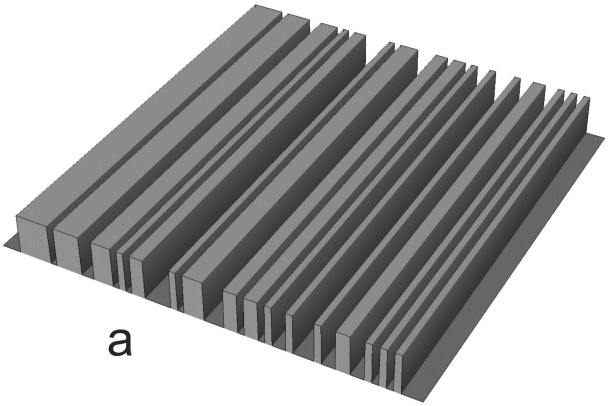

a

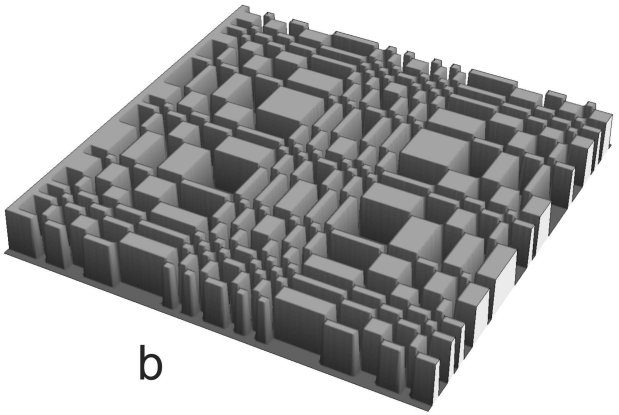

b

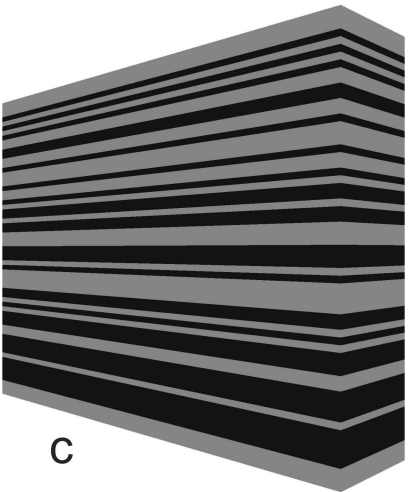

c

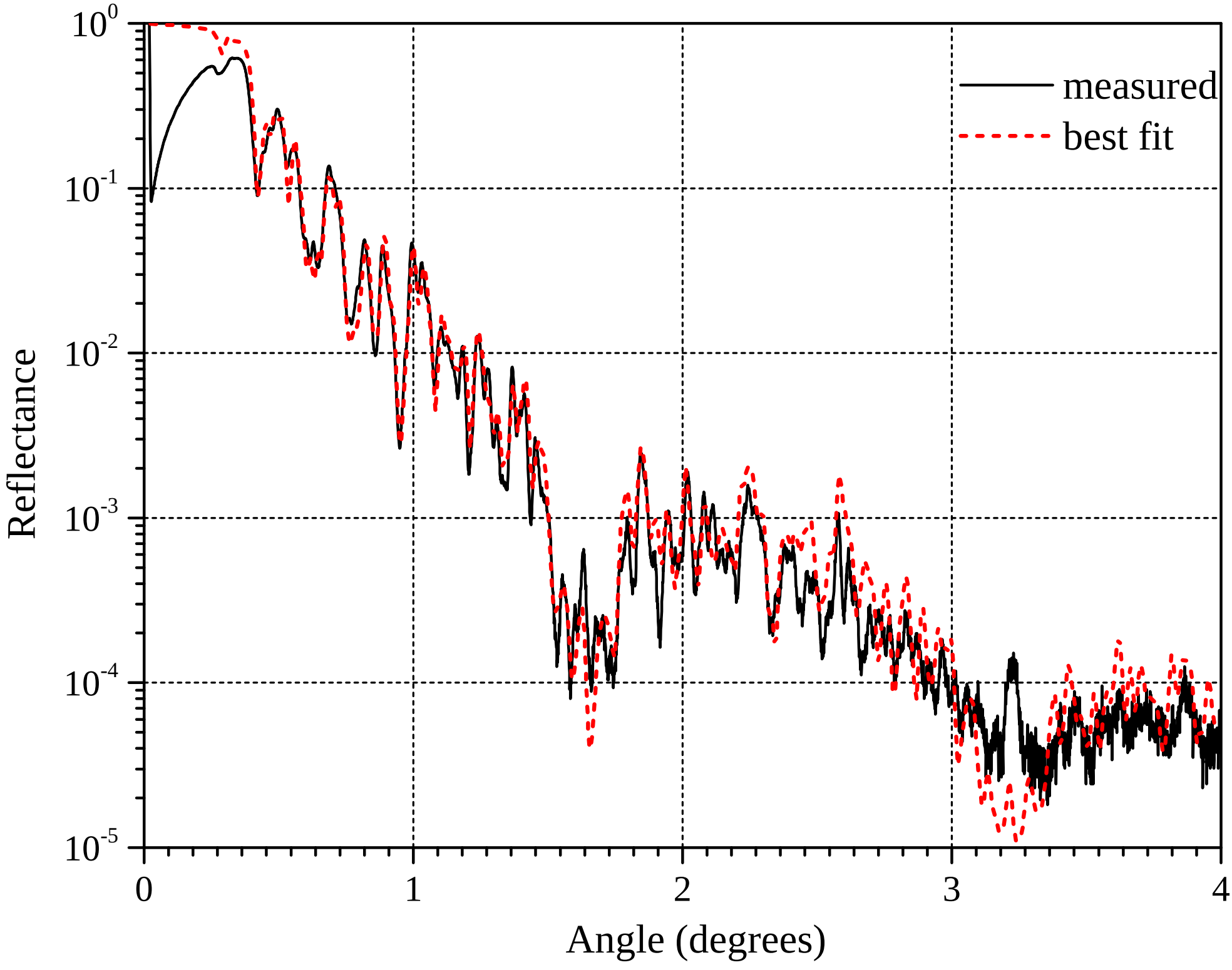
measured
best fit
Reflectance
Angle (degrees)
10^{0}
10^{-1}
10^{-2}
10^{-3}
10^{-4}
10^{-5}
0
1
2
3
4

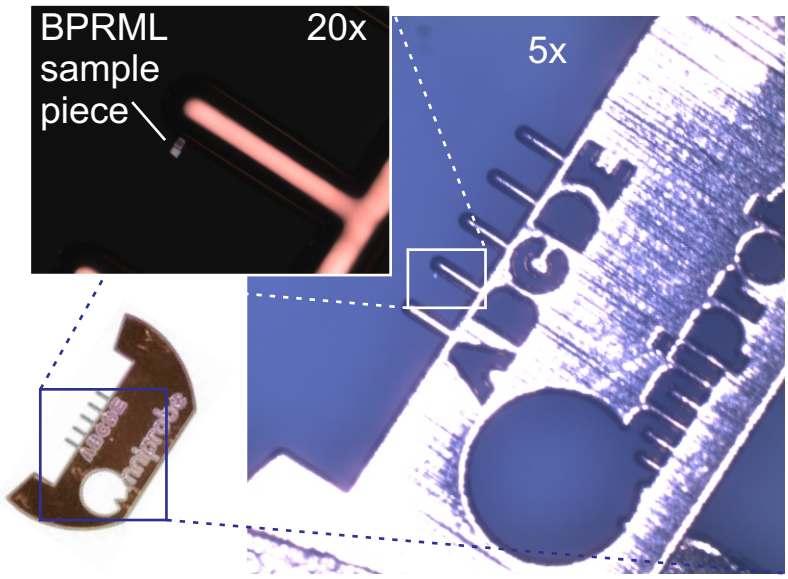
BPRML
sample
piece
20x
5x

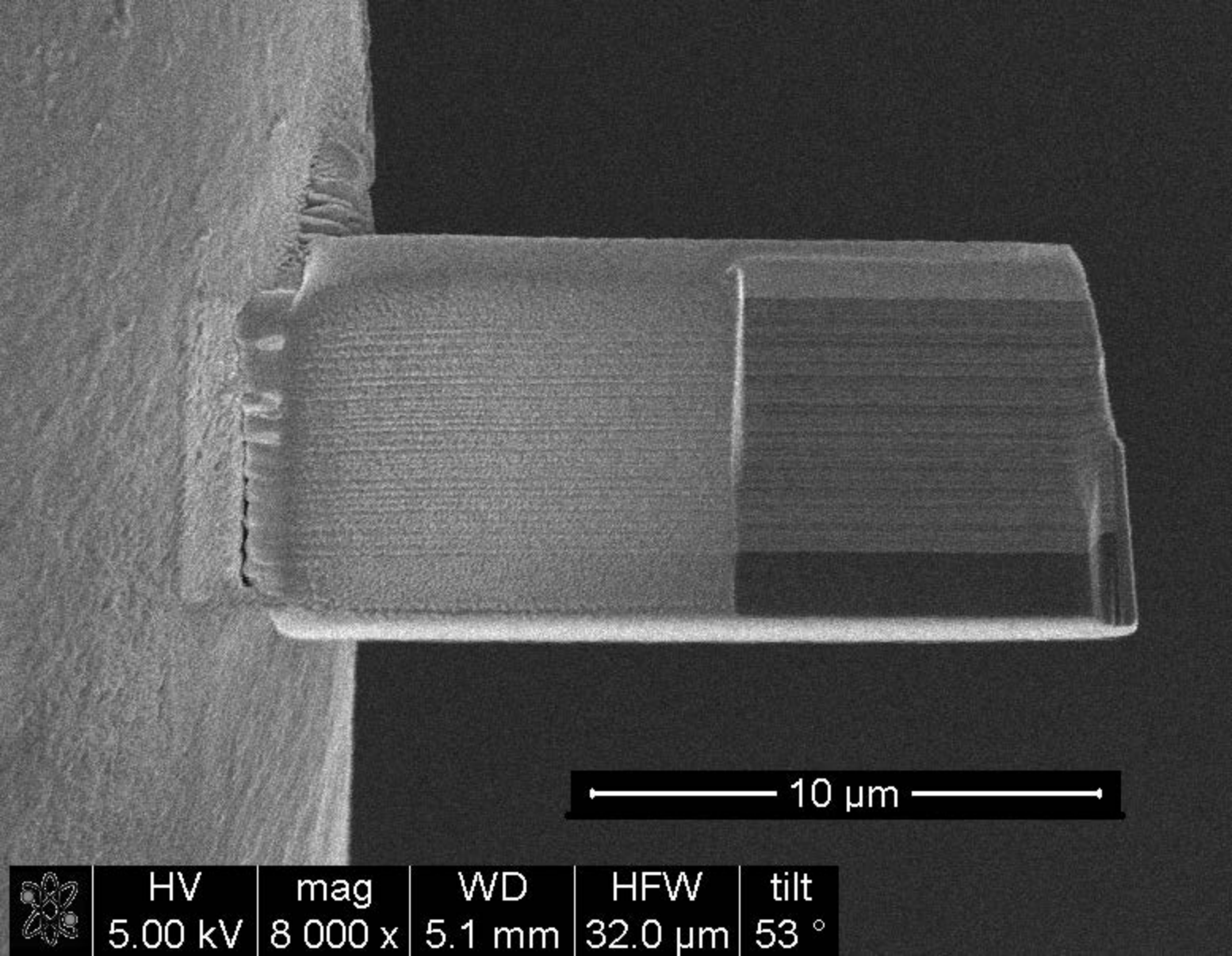
10 µm
HV
5.00 kV
mag
8 000 x
WD
5.1 mm
HFW
32.0 µm
tilt
53 °

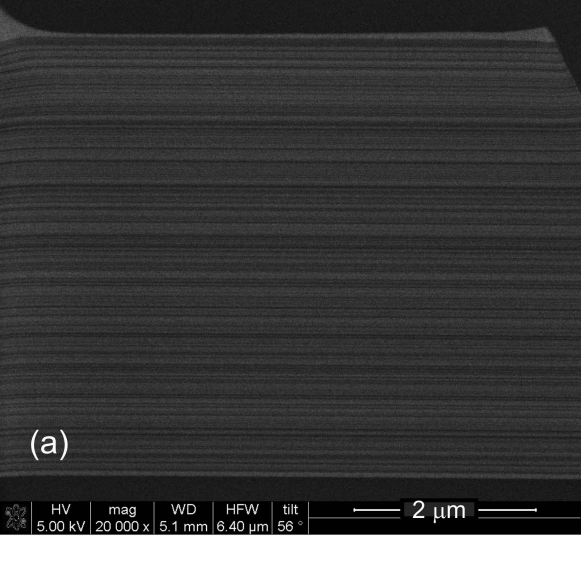
(a)
HV
5.00 kV
mag
20 000 x
WD
5.1 mm
HFW
6.40 µm
tilt
56 °
2 µm

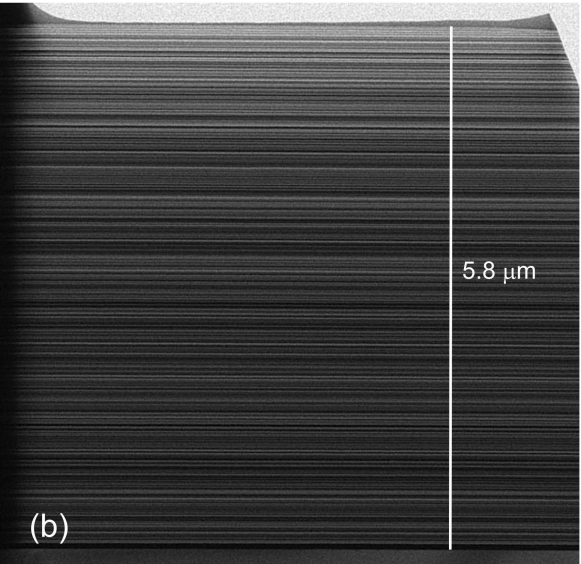
5.8 µm
(b)

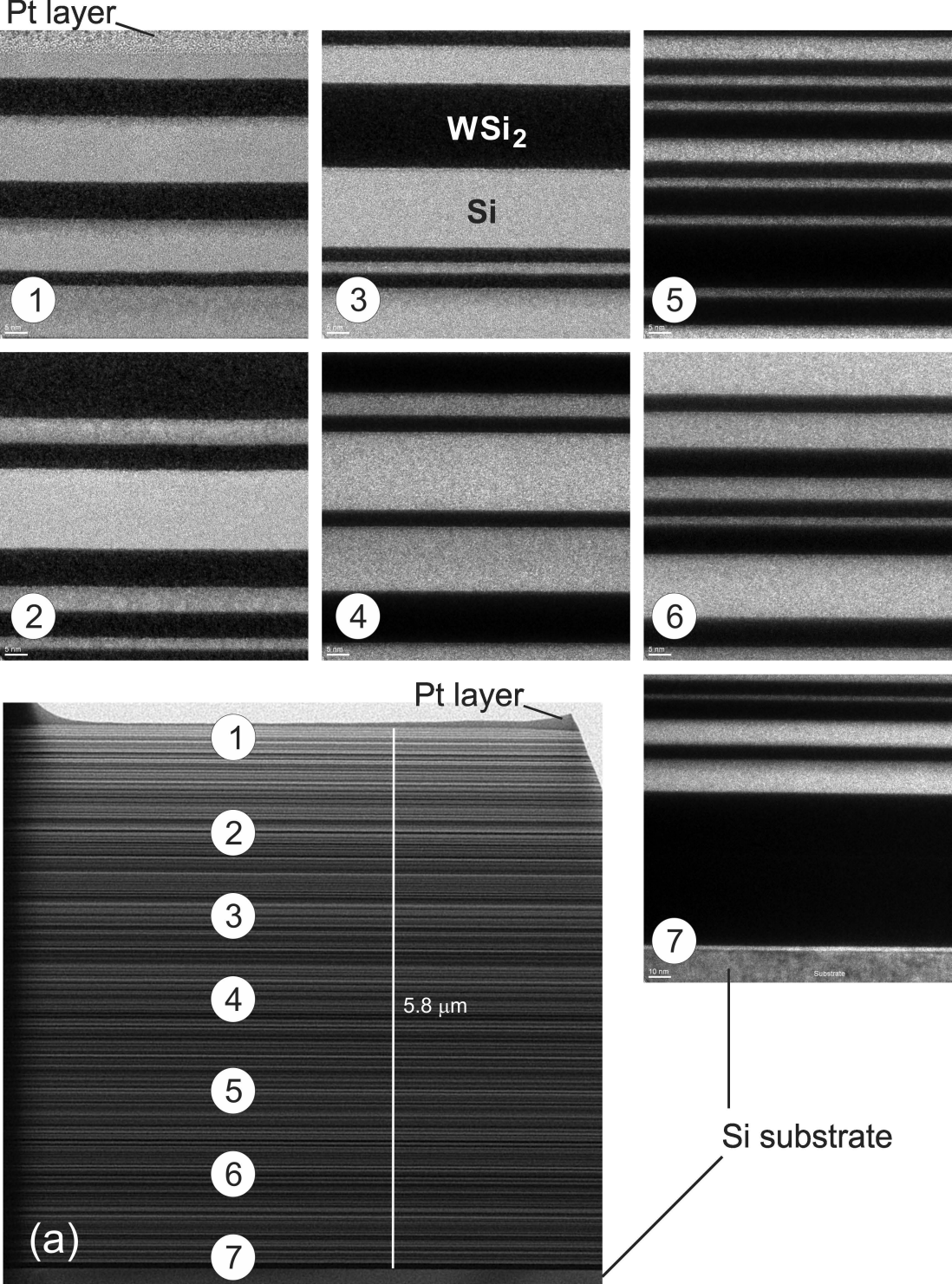
Pt layer
WSi2
Si
1
2
3
4
5
6
7
5 nm
10 nm
Substrate
Pt layer
5.8 μm
Si substrate
(a)

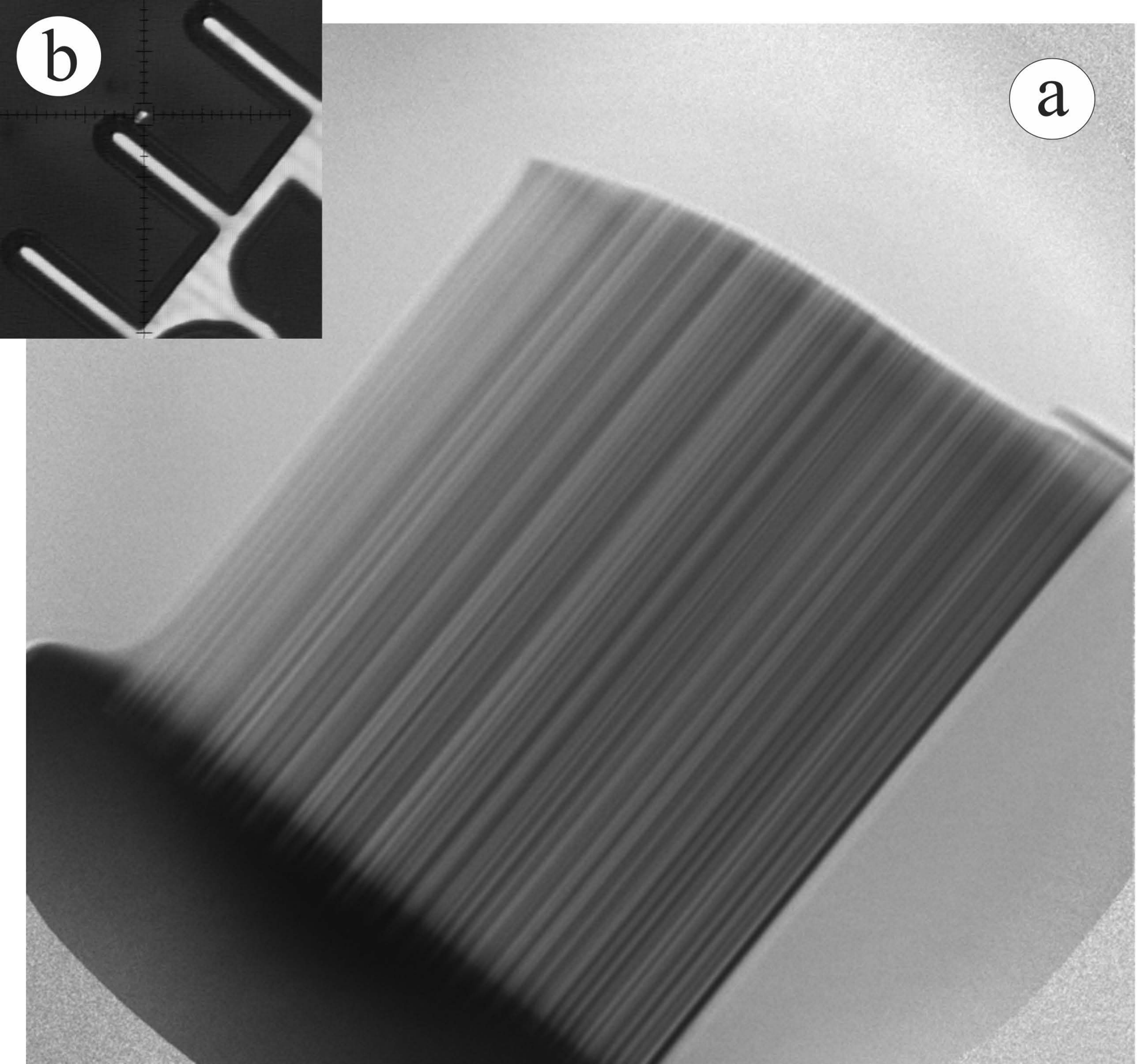
b
a

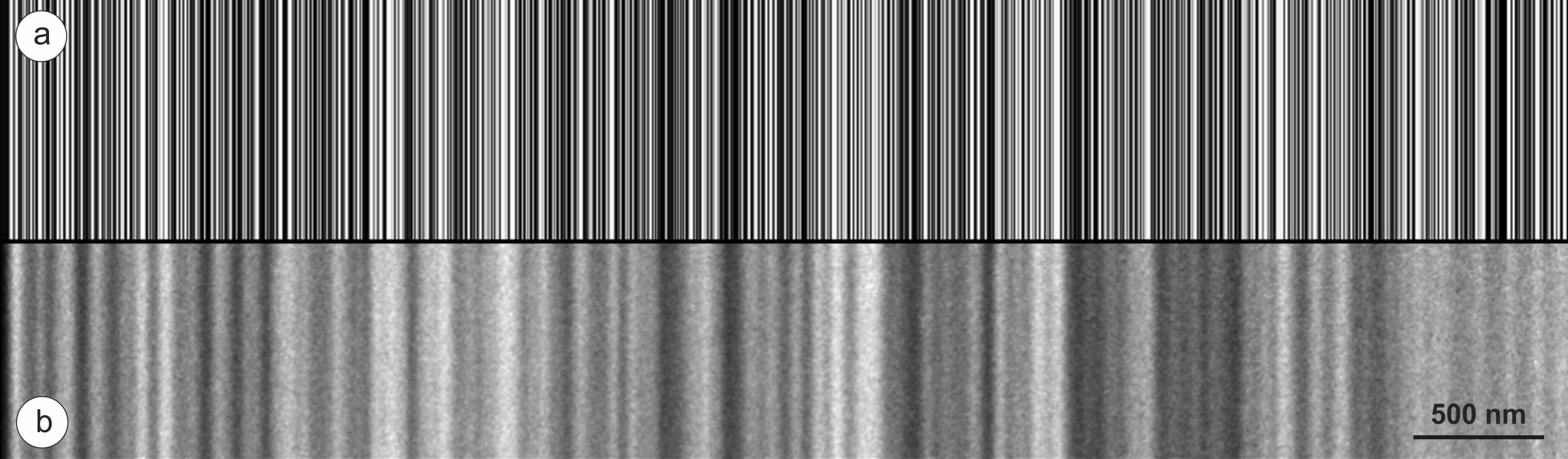
a
b
500 nm

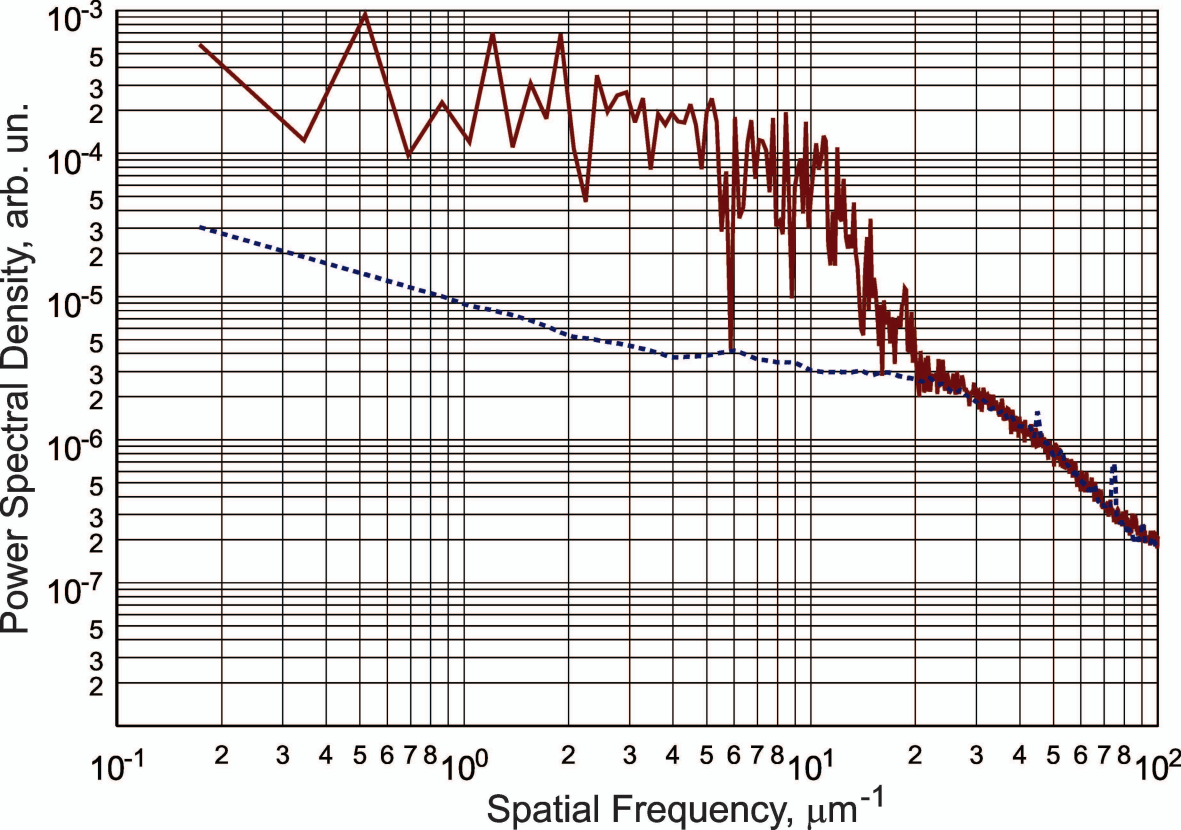
Power Spectral Density, arb. un.
10-3
5
3
2
10-4
5
3
2
10-5
5
3
2
10-6
5
3
2
10-7
5
3
2
10-1
2 3 4 5 6 7 8
100
2 3 4 5 6 7 8
101
2 3 4 5 6 7 8
102
Spatial Frequency, μm-1

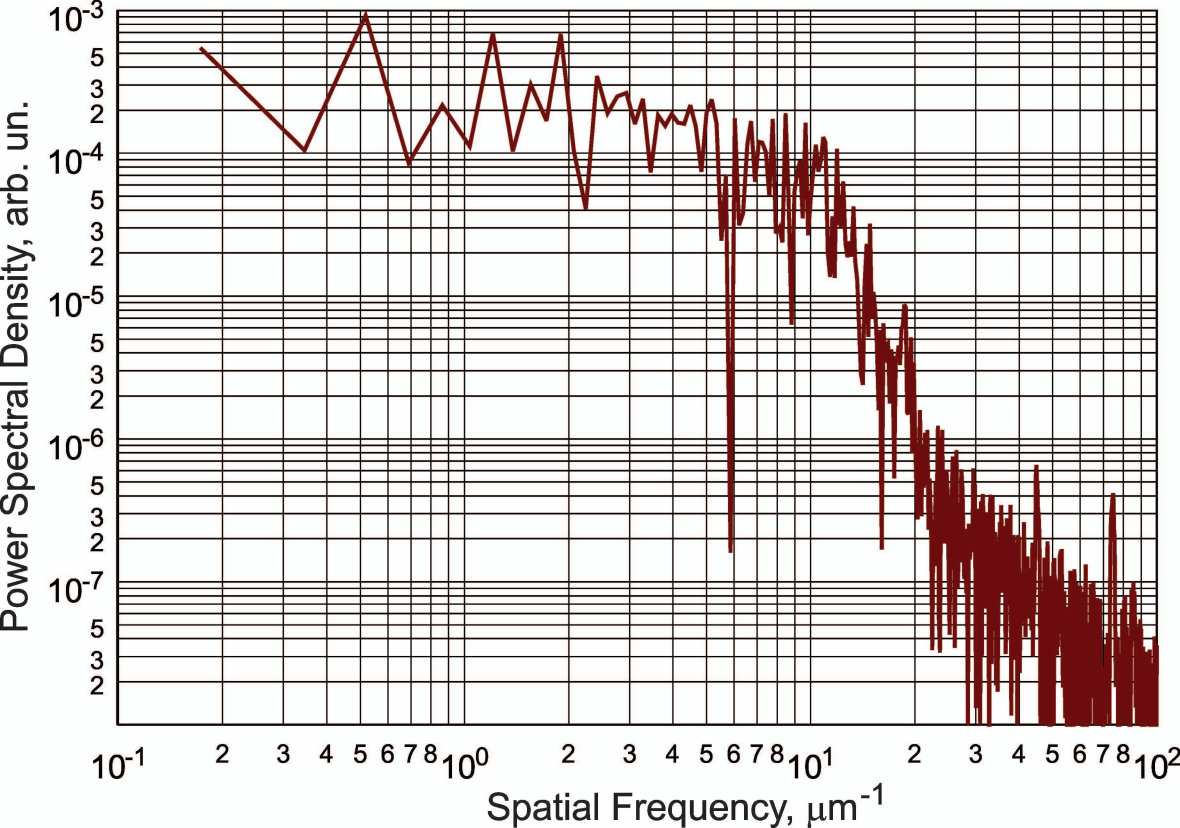
Power Spectral Density, arb. un.
10-3
5
3
2
10-4
5
3
2
10-5
5
3
2
10-6
5
3
2
10-7
5
3
2
10-1
2 3 4 5 6 7 8
100
2 3 4 5 6 7 8
101
2 3 4 5 6 7 8
102
Spatial Frequency, μm-1

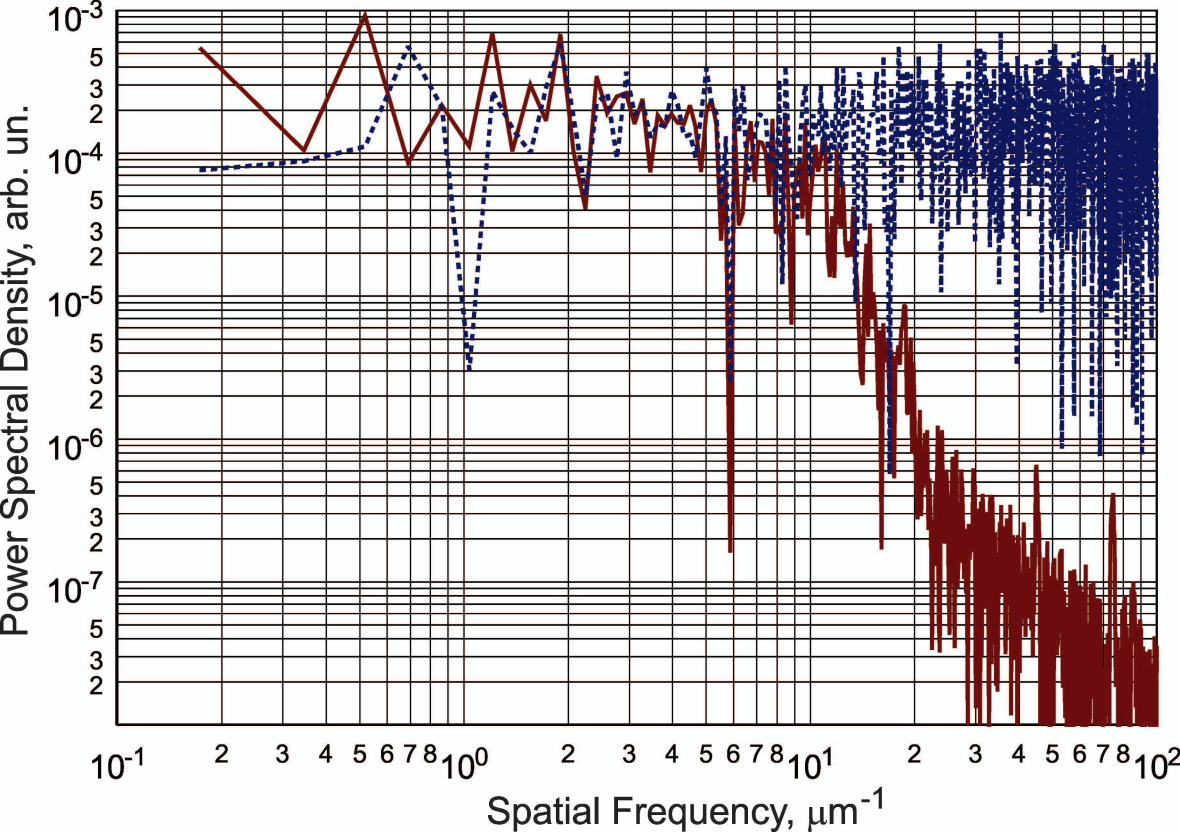
Power Spectral Density, arb. un.
10-3
5
3
2
10-4
5
3
2
10-5
5
3
2
10-6
5
3
2
10-7
5
3
2
10-1
2 3 4 5 6 7 8
100
2 3 4 5 6 7 8
101
2 3 4 5 6 7 8
102
Spatial Frequency, μm-1

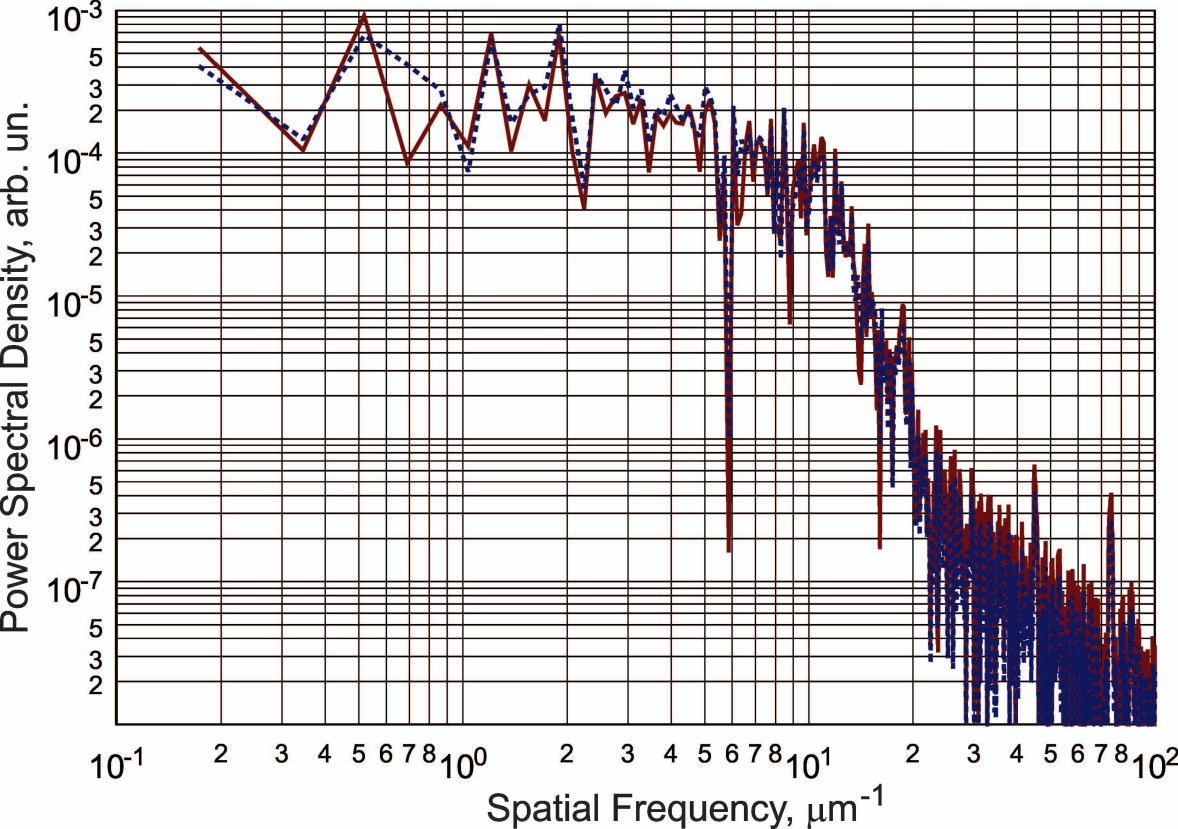
Power Spectral Density, arb. un.
10-3
5
3
2
10-4
5
3
2
10-5
5
3
2
10-6
5
3
2
10-7
5
3
2
10-1
2 3 4 5 6 7 8
100
2 3 4 5 6 7 8
101
2 3 4 5 6 7 8
102
Spatial Frequency, μm-1

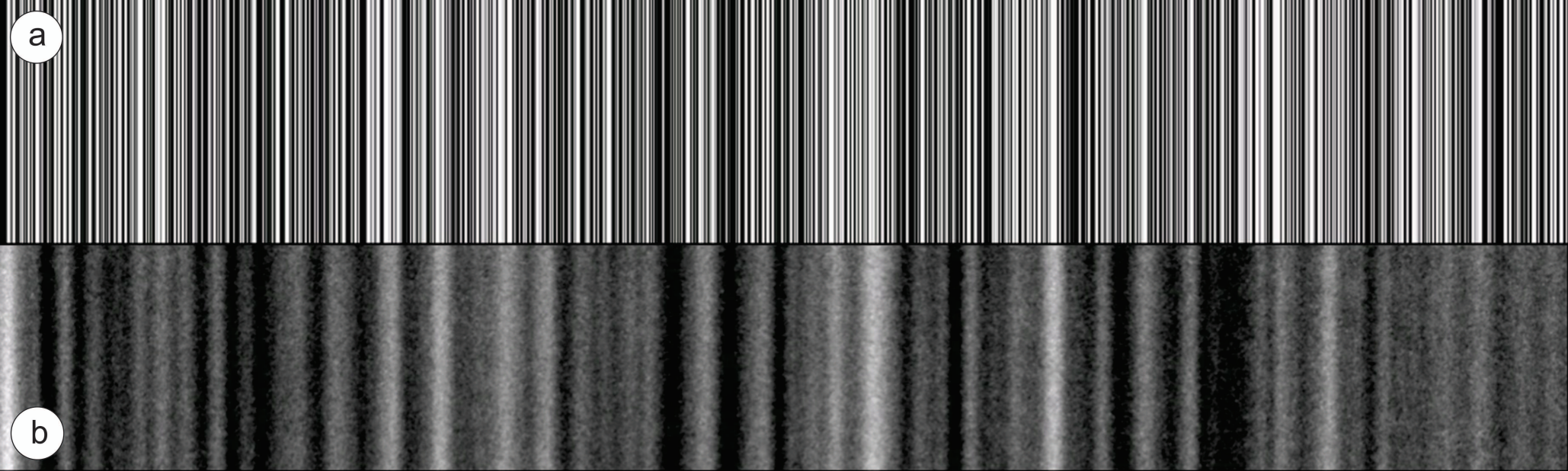
a
b

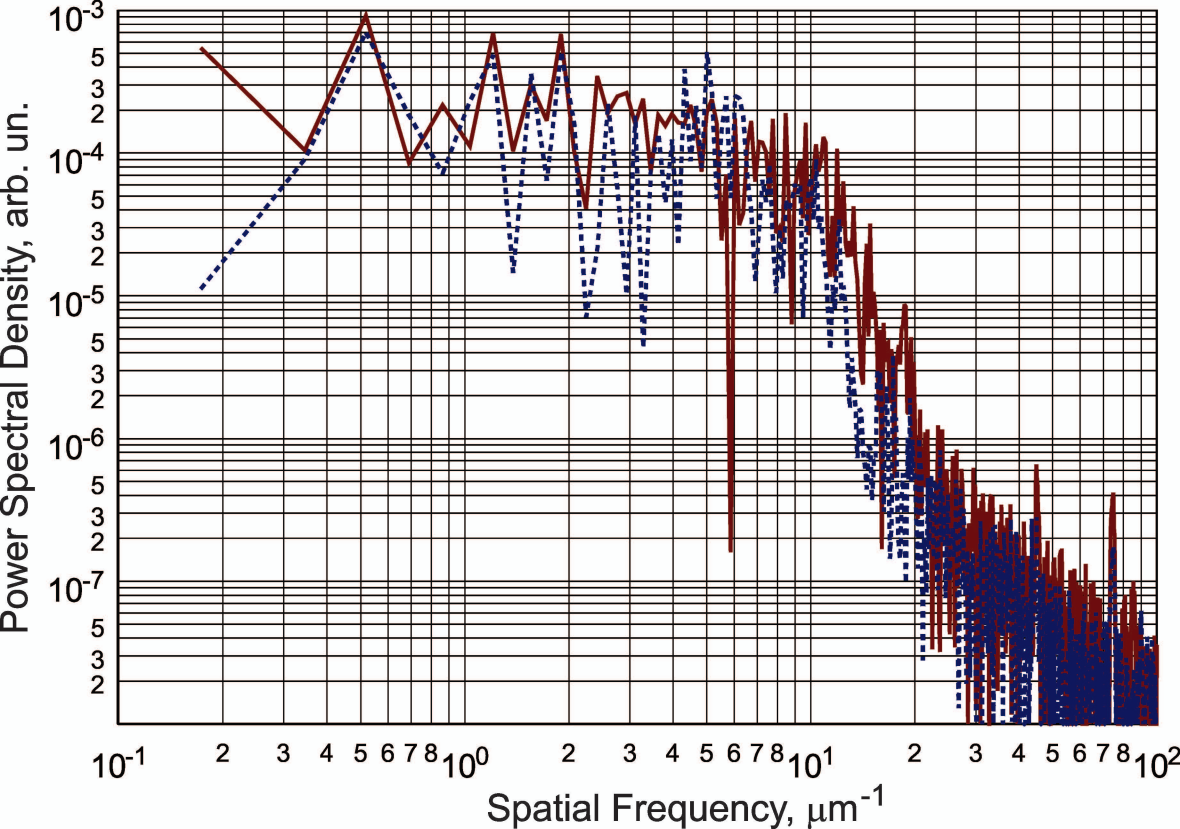
Power Spectral Density, arb. un.
10-3
5
3
2
10-4
5
3
2
10-5
5
3
2
10-6
5
3
2
10-7
5
3
2
10-1
2 3 4 5 6 7 8
100
2 3 4 5 6 7 8
101
2 3 4 5 6 7 8
102
Spatial Frequency, μm-1

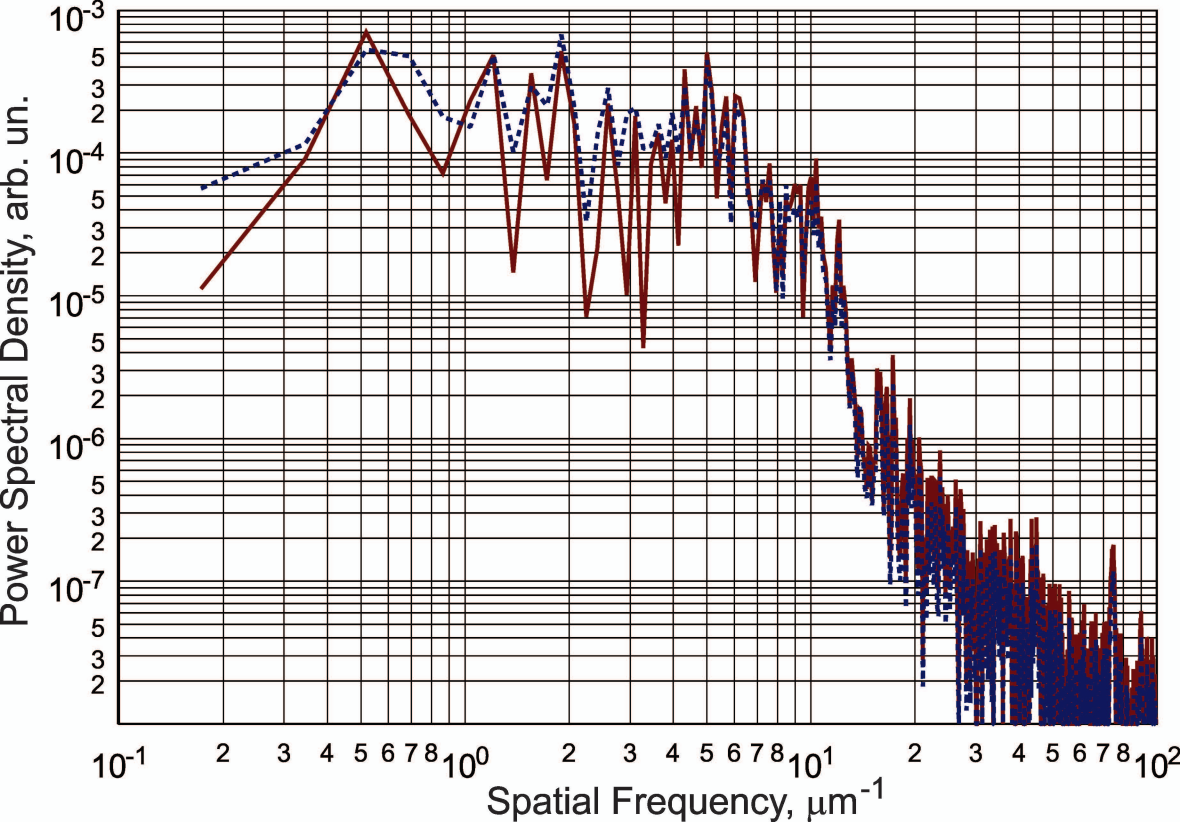
Power Spectral Density, arb. un.
10-3
5
3
2
10-4
5
3
2
10-5
5
3
2
10-6
5
3
2
10-7
5
3
2
10-1
2 3 4 5 6 7 8
100
2 3 4 5 6 7 8
101
2 3 4 5 6 7 8
102
Spatial Frequency, μm-1

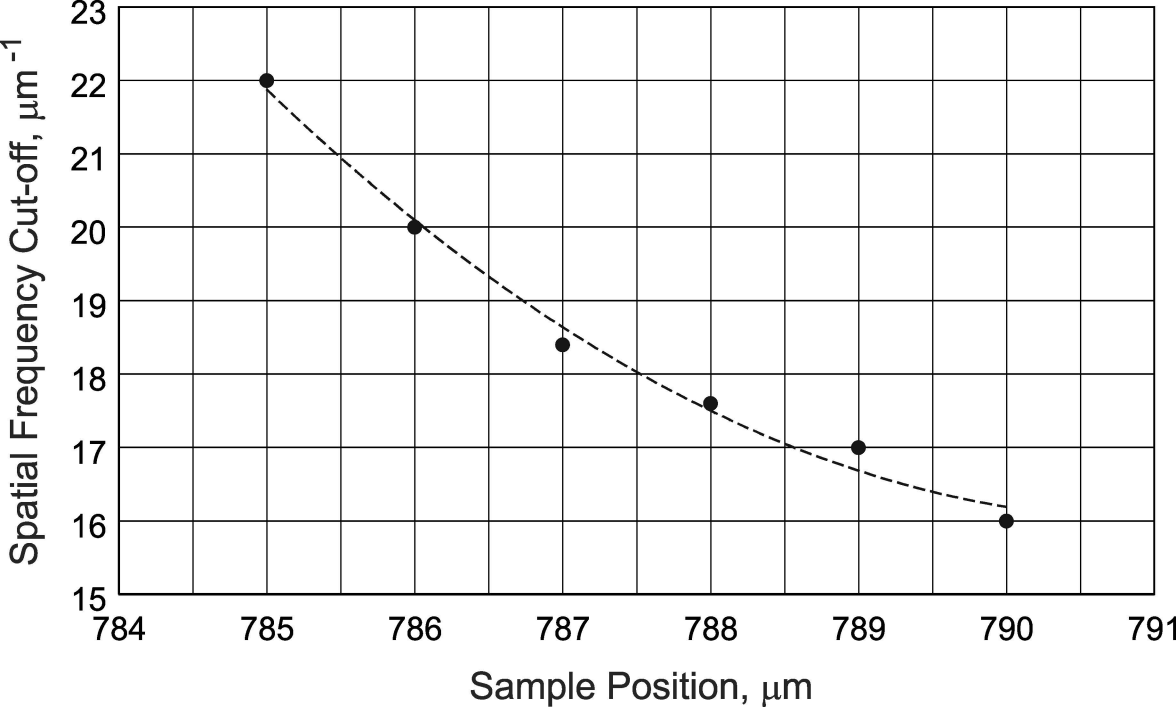
Spatial Frequency Cut-off, μm -1
23
22
21
20
19
18
17
16
15
784
785
786
787
788
789
790
791
Sample Position, μm